Engineering aspects of hypersonic turbulent flows at suborbital enthalpies

By J. Urzay AND M. Di Renzo†

1. Motivation and objectives

One of the least explored frontiers in aeronautics deals with hypersonic flight at low altitudes. In the terrestrial atmosphere, the three fundamental characteristics of airflows surrounding flight systems in this regime are:

- High freestream Reynolds numbers (sufficiently high to induce turbulent boundary layers around the fuselage).
- High freestream Mach numbers (sufficiently high to yield large normal Mach numbers and large recovery temperatures).
- High stagnation enthalpies (higher or much higher than the characteristic vibrational energies of the oxygen and nitrogen molecules).

Flight systems operating in the realm of this hypersonics trifecta are enveloped by turbulent, hot, highly compressible air in chemical nonequilibrium, subjected to strong two-way coupling with the thermal, chemical, and mechanical responses of the fuselage. In addition, because of the low altitudes involved, the airflow around the flight system may be laden with aerosols and particulates as a result of hypersonic navigation through weather systems such as dust storms and clouds of ice crystals and water droplets.

A practical consequence of this hypersonics trifecta is a large increase in heat loads on the airframe. This phenomenon is easily recognizable in post-flight inspections as a charred fuselage and is often associated with an impending *"heat barrier"* (von Kármán 1956). It is this risk of obliteration of the airframe by the heat barrier that aerospace engineers have leveraged over the last 60 years to design most high-speed flight systems to deliberately operate in conditions where, at most, only two characteristics of the hypersonics trifecta were simultaneously present, as shown in Figure 1. These operating conditions have involved (a) hypersonic flight at very high altitudes in the mesosphere and upper layers of the stratosphere, where the flow around the system is mostly laminar; and (b) subsonic and supersonic flight at low altitudes in the troposphere and lower stratosphere, where the flow around the system becomes turbulent.

There is, however, a clear consensus that the mostly unexploited regime of hypersonic flight at low altitudes bears strong potential for both military and civilian applications. Unfortunately, we know the least fundamentally about this regime. Our ignorance about it stems, in great part, from the still uncharted physical processes that set the thermomechanical loads on the airframe. One of these processes, which is the focus of this report, is the interaction between turbulence and thermochemical effects.

The rest of this report is organized as follows. Section 2 provides a short survey of the hypersonics trifecta in flight systems. Section 3 focuses on elementary aerothermochemical aspects of the problem. Section 4 devises interplays between turbulence and thermodynamic nonequilibrium effects in hypersonic boundary layers. Concluding remarks are provided in Section 5. Additionally, a formulation for wall-modeled Large-Eddy Simulations (LES) of hypersonic turbulent flows at high enthalpies is included in the Appendix.

---

† Presently at CERFACS, France.

A companion journal article (Di Renzo & Urzay 2021) provides details of the formulation and computational setup employed to obtain the Direct Numerical Simulation (DNS) results in Section 3, along with a complete description of first- and second-order statistics for all aerothermochemical variables. The discussion here contains supplementary data and many schematics not shown in that journal article, and provides a deeper focus on potential repercussions for modeling of hypersonic turbulent flows.

2. The hypersonics trifecta in flight trajectories

To understand the intellectual gap that exists in this research area, it is convenient to briefly highlight the disconnect between flight regimes within the realm of the hypersonics trifecta mentioned above and the corresponding state of the art in the fundamental knowledge of hypersonic turbulence available from basic but nonetheless fully resolved and well-controlled simulation studies. Several full-system simulation studies based on Reynolds-Averaged Navier-Stokes (RANS) models for hypersonic flows exist, although it appears that the rigor of these models would greatly benefit from narrowing this gap.

Manned spacecrafts re-entering the terrestrial atmosphere at Mach 25-40 from Low Earth Orbit (LEO) or lunar return in Figure 1 are characterized by very high stagnation enthalpies in the initial stages of their trajectories, but necessarily dissipate most of their orbital kinetic energy soon in the mesosphere to limit maximum accelerations. However, because of the high altitudes prevailing there, and because of their highly blunted geometries, these systems tend to be subjected to flows at low-to-transitional Reynolds numbers during the critical hypersonic segments of their trajectories.

Endo-atmospheric hypersonic airbreathing vehicles and rocket planes, which have only existed in testing phase to date, attain their maximum speed of Mach 5-10 within the stratosphere and are therefore subjected to comparatively larger Reynolds numbers typical of turbulent regimes, although the corresponding stagnation enthalpies are much smaller than those of re-entering spacecrafts. Important systems not shown in Figure 1, such as nose cones of intercontinental ballistic missiles (ICBMs), must operate with steep trajectories at high Mach numbers of 10-20 in their terminal phase within the troposphere to avoid antiballistic interceptors, and are therefore subjected to very high Reynolds numbers near the ground and to stagnation enthalpies higher than those of endo-atmospheric hypersonic airbreathing vehicles, albeit for a shorter time.

According to publicly available sources (Sayler 2020), modern designs of hypersonic weapon systems involve (a) trans-atmospheric hypersonic gliders capable of skipping during re-entry for long downrange distances, and (b) endo-atmospheric airbreathing hypersonic cruise missiles based on scramjets capable of level powered flight at stratospheric or tropospheric altitudes. Keystone capabilities envisioned for both of these systems, which fundamentally set them apart from conventional strike systems, are their guided hypersonic-speed crossrange maneuverability near the ground in their terminal phase while approaching the target by grazing the curved surface of the Earth to remain in the shadow of ground radars for the longest possible time. Similarly, linear or centrifugal hypervelocity accelerators for surface-to-space launch systems under commercial development will involve projectiles or payloads traversing the troposphere at near-orbital speeds, or equivalently, Mach 25. As the tendency to minimize flight times continues by pursuing increasingly higher velocities at increasingly lower altitudes, these systems will have to contend with increasingly more severe challenges associated with the heat barrier, including interactions between turbulence and thermochemical effects.

Most of the recent computational work on fundamental aspects of hypersonic aerody-

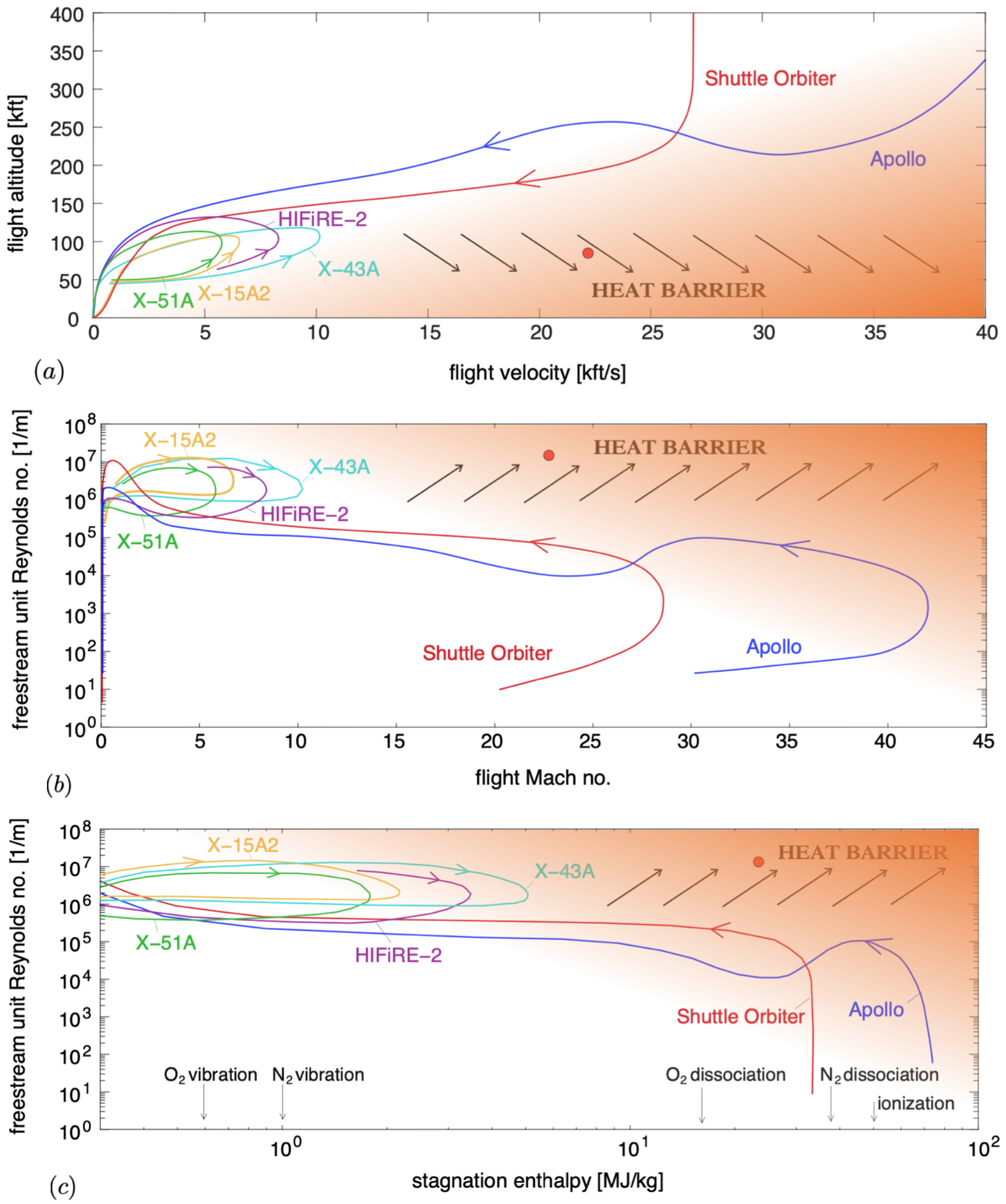

FIGURE 1. Flight trajectories of relevant hypersonic flight systems in terms of (a) flight velocity versus altitude, (b) flight Mach number versus freestream unit Reynolds number, and (c) stagnation enthalpy versus freestream unit Reynolds number. These trajectories have been reconstructed using the US Standard Atmosphere model and flight data from Hillje (1969) for the Apollo Command Module, Goodrich *et al.* (1983) for the Shuttle Orbiter, Marshall *et al.* (2005) for the X-43A, Jackson *et al.* (2015) for HIFiRE-2, Watts (1968) for the X-15A2, and Hank *et al.* (2008) for the X-51A. The vertical arrows in panel (c) indicate characteristic energies of ionization, dissociation and vibrational excitation. The realm of the hypersonics trifecta is denoted by the shaded area. The solid red dots indicate the equivalent freestream (pre-shock) conditions corresponding to the simulations in Di Renzo & Urzay (2021).

namics has been focused on flows in which only two of the three characteristics of the hypersonics trifecta were simultaneously present. A nonexhaustive list of those studies includes (a) hypersonic transitional and turbulent boundary layers of calorically perfect gases (Franko & Lele 2013; Zhang *et al.* 2018; Hader & Fasel 2019; Thome *et al.* 2019; Fu *et al.* 2021), and (b) hypersonic laminar and transitional boundary layers of inert thermally perfect gases and of high-temperature chemically reacting gases (Marxen *et al.* 2014; Mortensen & Zhong 2016; Colonna *et al.* 2019; Chen & Boyd 2020).

Much more scarce are direct numerical simulations (DNS) of hypersonic boundary layers at high enthalpies and sufficiently high Reynolds numbers for the flow to become turbulent. This class of studies includes the pioneering investigation by Duan & Martin (2011*a*) of temporally evolving boundary layers, and the more recent study by Di Renzo & Urzay (2021) of a Mach-10 spatially evolving boundary layer. These simulations have been focused only on idealized flat plates subjected, at most, to chemical surface catalysis.

Validation of these fundamental DNS studies is still largely precluded by experimental limitations in both diagnostics and operability of wind tunnels in conditions warranting turbulence, hypersonic speeds, and high stagnation enthalpies. Note that blowing air in standard ground facilities at conditions representative of low-altitude hypersonic flight requires a very large amount of flow power comparable to the stagnation enthalpy flux across the test section. For instance, accelerating air to Mach 23 in a wind tunnel test section of 30 cm in diameter, while reproducing the temperature and density at an altitude of 25 km in the lower stratosphere, requires a flow power on the order of

$$\begin{aligned} &\text{density} \times \text{velocity} \times \text{stagnation enthalpy} \times \text{area} \\ &\qquad = \left(0.04\ \text{kg/m}^3\right)(6.74\ \text{km/s})(21.6\ \text{MJ/kg})\left(0.07\ \text{m}^2\right) = 407\ \text{MW}, \end{aligned}$$

which corresponds to approximately 35% of the electric power output of one of the two reactors in the Diablo Canyon nuclear power plant serving the entire state of California. These limitations are compounded by challenges associated with the utilization of laser diagnostics to measure flow quantities in thin near-wall regions concealed in the hypersonic boundary layer surrounding the flight system, where most interactions between turbulence and thermochemical effects take place. As a result, even the most basic characteristics of turbulent flows at these extreme conditions remain undiscovered.

3. Hypersonic boundary layers around flight systems in the lower stratosphere

Consider Figure 2 as a prototypical example of a gas environment around a hypersonic flight system in the low stratosphere, where a 9° wedge flying at Mach 23 at an altitude of 25 km is sketched, which corresponds to the same conditions simulated in Di Renzo & Urzay (2021). In the latter study, a DNS computational domain composed of 2.1 billion grid elements was used that was limited to a small region downstream of the shock and is denoted in Figure 2 by the dashed cuboid bounded by $x_o = 65\delta_o^\star = 14$ mm, $x_1 = 1865\delta_o^\star = 399$ mm, $y_o = 0$, $y_1 = 75\delta_o^\star = 16$ mm, $z_o = 0$, and $z_1 = 20\pi\delta_o^\star = 13$ mm. In this notation, $\delta_o^\star = 0.2$ mm is the displacement thickness of the laminar boundary layer entering the domain, which is equivalent to a 99%-thickness $\delta_0^{99} = 0.3$ mm.

3.1. *Overall description of the hypersonic boundary layer*

At this altitude and flight velocity, the unit Reynolds number in the free stream is $18 \cdot 10^6\ \text{m}^{-1}$, and the resulting stagnation enthalpy is 21.6 MJ/kg. These conditions are indicated in each panel of Figure 1 by the solid red dots. In particular, this stagnation enthalpy is smaller than the dissociation energy of N_2, 37 MJ/kg, but larger than the

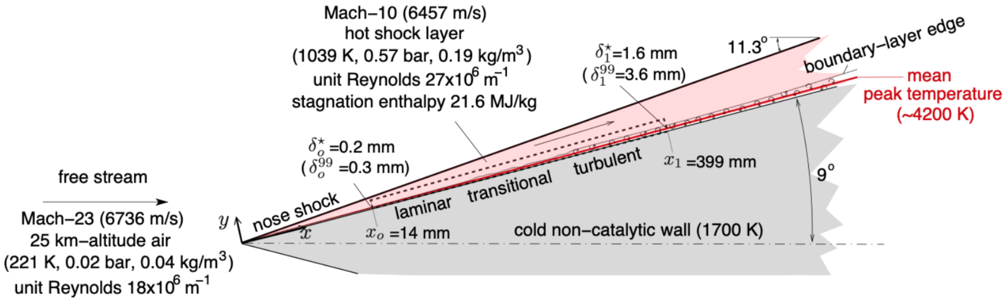
Mach–10 (6457 m/s)
hot shock layer
(1039 K, 0.57 bar, 0.19 kg/m^3)
unit Reynolds 27x10^6 m^{-1}
stagnation enthalpy 21.6 MJ/kg
$\delta_1^\star$=1.6 mm
(δ_1^{99}=3.6 mm)
11.3°
boundary–layer edge
mean
peak temperature
(~4200 K)
$\delta_o^\star$ =0.2 mm
(δ_o^{99} =0.3 mm)
free stream
Mach–23 (6736 m/s)
25 km–altitude air
(221 K, 0.02 bar, 0.04 kg/m^3)
unit Reynolds 18x10^6 m^{-1}
y
x
nose shock
laminar
transitional
turbulent
x_1 =399 mm
9°
x_o =14 mm
cold non–catalytic wall (1700 K)

FIGURE 2. Configuration schematics.

dissociation energy of O_2, 15 MJ/kg. It is also much larger than the characteristic vibrational energies of N_2 and O_2, which approximately correspond, respectively, to 1 MJ/kg and 0.6 MJ/kg. As a result, the flow near the wall attains thermal enthalpies leading to significant vibrational excitation of N_2 and O_2 molecules, along with values of molar fractions of O and NO within the ranges of 0.04 to 0.07 and 0.01 to 0.04, respectively. Specifically, the production of NO occurs thermally by the Zel'dovich mechanism activated by a temperature overshoot near the wall, whose origin is explained below. In contrast, the N_2 molecules do not dissociate as much. As a result, N is found in trace amounts of order 10^{-4} in molar fraction and remains close to steady state. However, these results rely on the chemical mechanism for high-temperature air provided by Park (1989) and on the assumption of thermodynamic equilibrium. Improvements to these simulations that may be worth pursuing involve (a) the utilization of updated dissociation mechanisms that account for vibrationally excited states (Chaudhry *et al.* 2020; Finch *et al.* 2020; Stretcher *et al.* 2020), and (b) the consideration of thermodynamic nonequilibrium effects (Singh & Schwartzentruber 2017). Effects introduced by the latter on hypersonic turbulent boundary layers are briefly discussed in Section 4.

Because of the high Mach numbers, a shock wave emanates from the vertex and closely envelops the wedge. The incidence angle of this shock is approximately 11.3° when the theory for calorically perfect gases is employed and viscous-inviscid interactions are neglected. Despite the slenderness of the wedge, the normal Mach number is 4.5, which is sufficiently high to produce large jumps in temperature, pressure, and density across the nose shock that fundamentally characterize inviscid hypersonic flow regimes. Specifically, the nose shock deflects the free stream and leaves behind hot air flowing hypersonically parallel to the surface at Mach 10 in a shock layer whose static pressure and temperature are, respectively, 0.57 bar and $T_e = 1039$ K, the latter being sufficient to partially activate molecular degrees of vibrational motion in N_2 and O_2 molecules in the inviscid bulk of the shock layer, but insufficient to dissociate them. However, viscous friction induces very high temperatures in the boundary layer that activate air dissociation. In particular, as observed in all practical flight scenarios, the cold temperature of the wall relative to the freestream stagnation temperature leads in the present configuration to a thin region parallel to the wall and concealed in the boundary layer, where aerodynamic heating by viscous friction occurs and the Favre-averaged temperature is maximum.

The wall temperature chosen for the reference configuration in Figure 2 is 1700 K, which corresponds to 7% of the stagnation temperature for a calorically-perfect diatomic gas. In addressing the practicality of this wall temperature, note that it represents a relatively high temperature that is well beyond creep limits for standard materials such

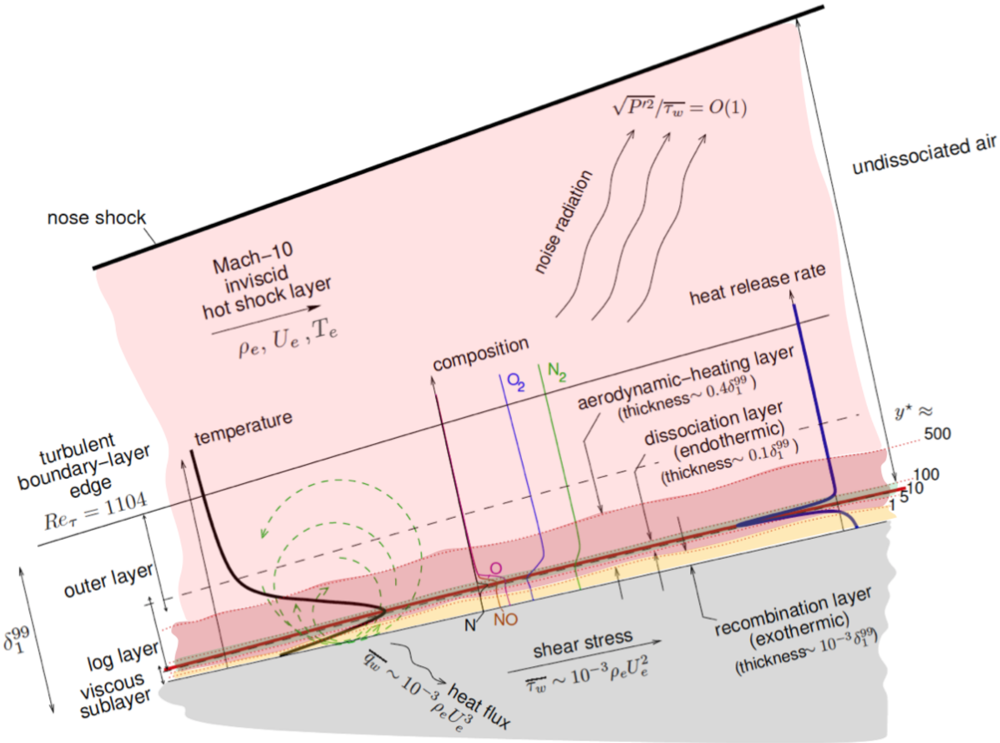
nose shock
$\sqrt{\overline{P'^2}}/\overline{\tau_w} = O(1)$
undissociated air
Mach–10
inviscid
hot shock layer
ρ_e, U_e, T_e
noise radiation
heat release rate
composition
O_2
N_2
aerodynamic–heating layer
(thickness$\sim 0.4\delta_1^{99}$)
dissociation layer
(endothermic)
(thickness$\sim 0.1\delta_1^{99}$)
$y^\star \approx$
500
100
10
5
1
temperature
turbulent
boundary–layer
edge
$Re_\tau = 1104$
outer layer
δ_1^{99}
log layer
viscous
sublayer
O
N
NO
$\overline{q_w} \sim 10^{-3} \rho_e U_e^3$
heat flux
shear stress
$\overline{\tau_w} \sim 10^{-3} \rho_e U_e^2$
recombination layer
(exothermic)
(thickness$\sim 10^{-3}\delta_1^{99}$)

FIGURE 3. Schematics of the structure of the hypersonic turbulent boundary layer.

as stainless steel or the early heat-resistant alloy Inconel-X used for the X-15. However, this wall temperature is within the operating thermomechanical limits of the advanced titanium-zirconium-molybdenum (TMZ) alloys used in the reusable heat shields of the X-20 Dynasoar and ASSET vehicles (Happenheimer 2007).

In the turbulent portion of the boundary layer, the maximum value of the Favre-averaged temperature in the aerodynamic-heating layer, $\widetilde{T}_{max} = 4200$ K, is attained in the buffer zone at a wall-normal semi-local distance of $y^\star = 10$, as indicated in Figure 2. In this notation, $y^\star$ represents the wall-normal distance y normalized with the inner semi-local unit $\overline{\mu}/[\overline{\rho}(\overline{\tau_w}/\overline{\rho})^{1/2}]$, where $\overline{\rho}$, $\overline{\mu}$, and $\overline{\tau_w}$ are the local mean values of density, dynamic viscosity, and wall shear stress, respectively. The gas in the vicinity of this temperature peak is characterized by the presence of the dissociation products O, NO, and – to a much lesser extent – N, as depicted in Figure 3. The dissociation of O_2 and the formation of NO near the temperature peak occurs under convectively supersonic flow containing velocity fluctuations that are sufficiently high to render a local turbulent Mach number of 0.8. The convective sonic line is located deep in the boundary layer within the viscous sublayer at $y^\star = 4$. Recombination of O and N occurs within this subsonic region in an even thinner layer adjacent to the wall at $y^\star \leq 1$.

In this report, terminology borrowed from the theory of incompressible turbulent boundary layers, such as outer, inner, log, and viscous layers, is employed to provide a comfortable reference of where the different physical processes dominate in the boundary layer. However, this implies that there exists a transformed mean velocity profile in this problem that does not differ fundamentally from that of an incompressible turbulent boundary layer. This is approximately – but certainly not exactly – true, as discussed in

Di Renzo & Urzay (2021). Velocity transformations for high-speed turbulent boundary layers have so far been studied only for calorically perfect gases.

The unit Reynolds number in the shock layer is $27 \cdot 10^6$ m^{-1}. Note that this value is larger than that in the pre-shock gas because of the moderately shallow incidence angle of the nose shock, which leaves behind high-temperature gas flowing still fast at a hypersonic edge Mach number. The boundary layer developing over the wedge is initially laminar and becomes turbulent by mechanisms whose detailed description is not relevant to the present discussion. In practical flight scenarios, these transition mechanisms, separately or combined, involve (a) natural growth of instabilities, (b) receptivity to freestream disturbances, (c) boundary-layer reattachment downstream of incident shocks or unevenly joined airframe panels or heat-shield tiles, (d) surface roughness induced by surface finish or erosion by atmospheric particulates, and (e) large-scale surface deformation induced by ablation of the thermal shield or by internal thermal stresses caused by aerodynamic heating and wall catalysis. In this report, transition is numerically induced by a suction-and-blowing wall boundary condition that is imposed on a thin spanwise strip approximately 1 mm wide located between $x = 17$ mm and $x = 18$ mm along the wall. The resonance between high-order oblique modes and the leading-order two-dimensional mode (similar to the second Mack mode arising in high-speed transition of calorically perfect gases), along with the subsequent growth of a secondary instability, lead to transition to turbulence at approximately $x_t = 291$ mm from the wedge vertex.

Transition is accompanied by increments in wall friction and heating by factors of approximately 4 and 5, respectively, as indicated in Figure 4. Whereas there exist correlations and analogies for the skin friction coefficient and Stanton number for compressible turbulent boundary layers of calorically perfect gases, the corresponding state of the art for high-enthalpy hypersonic turbulent boundary layers is comparatively barren.

The turbulent boundary layer exiting the domain has a displacement thickness $\delta_1^\star =$ 1.6 mm, which is equivalent to a 99%-thickness $\delta_1^{99} = 3.6$ mm. There, the mean values of the wall heat flux and wall shear stress are $\overline{q_w} = 11$ MW/m^2 and $\overline{\tau_w} = 3.1$ kPa, respectively. The wall heat flux corresponds to 4% of the stagnation enthalpy flux, or equivalently, to approximately three times the peak wall heat flux on the Apollo capsule during re-entry, and to approximately 10% of the peak wall heat flux during the re-entry of an ICBM nose cone (Urzay 2020). The wall shear stress represents 20% of the rms of the static pressure fluctuations acting normally to the wall. Consequently, the total fluctuating stress acting normally to the wall has a maximum value of 72 kPa.

The rms of the pressure fluctuations radiated from the turbulent boundary layer is approximately $2\overline{\tau_w}$, thereby inducing a local sound pressure level of 170 dB. Methods for suppressing such high sound pressure levels radiated from high-enthalpy hypersonic turbulent boundary layers enveloping the fuselage, along with the strong boom that would be created near the ground by the decaying nose shock, may be important subjects for future research to improve the feasibility (for civilian applications) and stealth characteristics (for military applications) of low-altitude hypersonic flight systems.

3.2. *Streamwise evolution of selected quantities*

Besides providing the distributions of different definitions of the Reynolds number along the entire boundary layer, Table 1 reveals the following aspects about the thermochemical structure of the boundary layer that may be of some relevance for subgrid-scale (SGS) modeling or for guiding grid-resolution requirements:

- The peak Favre-averaged temperature $\widetilde{T}_{max}$ decreases during transition, but increases after transition is completed around $\hat{x} \approx 1300$ in Figure 4 (or equivalently,

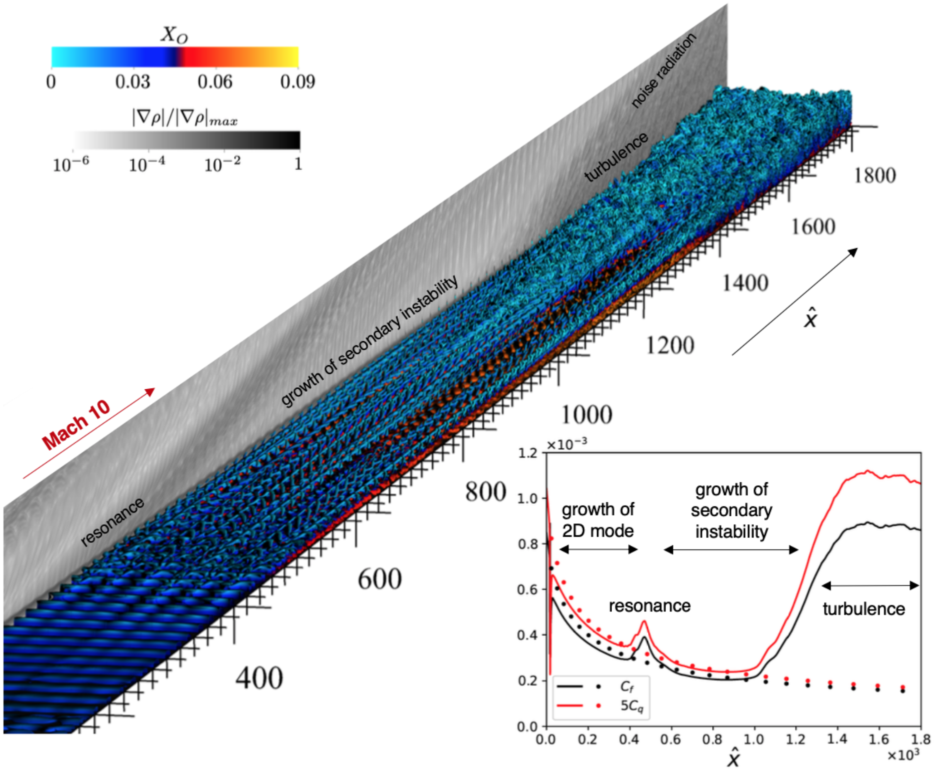
X_O
0
0.03
0.06
0.09
$|\nabla\rho|/|\nabla\rho|_{max}$
10^{-6}
10^{-4}
10^{-2}
1
noise radiation
turbulence
growth of secondary instability
Mach 10
resonance
1800
1600
1400
1200
1000
800
600
400
$\hat{x}$
$\times10^{-3}$
1.2
1.0
0.8
0.6
0.4
0.2
0.0
growth of 2D mode
growth of secondary instability
resonance
turbulence
C_f
$5C_q$
0.0
0.2
0.4
0.6
0.8
1.0
1.2
1.4
1.6
1.8
$\times10^{3}$
$\hat{x}$

FIGURE 4. DNS of a Mach-10 hypersonic transitional boundary layer. The figure shows instantaneous isosurfaces of the Q invariant colored by the molar fraction of O. The side plane is colored by the magnitude of the density gradient normalized by its maximum value. The inset shows the distribution of the skin friction coefficient $C_f = 2\overline{\tau_w}/(\rho_e U_e^2)$ and the dimensionless wall heat flux $C_q = \overline{q_w}/(\rho_e U_e^3)$, both of which are based on the edge (post-shock) density ρ_e and velocity U_e. The symbol $\hat{x} = (x - x_o)/\delta_o^\star$ is the streamwise coordinate measured from the inlet domain location x_o and nondimensionalized with the displacement thickness of the inflow boundary layer $\delta_o^\star$. Solid lines indicate DNS results, whereas the symbols correspond to the solution of the locally self-similar, laminar boundary layer. Results adapted from Di Renzo & Urzay (2021) and computed using the Hypersonics Task-based Research (HTR) solver (Di Renzo *et al.* 2020).

$x \approx x_t = 291$ mm). However, the maximum variations of $\widetilde{T}_{max}$ along the boundary layer are small and only amount to approximately 360 K.

- $\widetilde{T}_{max}$ is everywhere significantly smaller than the value $\widetilde{T}_{max} = 6.52T_e = 6826$ K predicted by the Crocco-Busemann equation for calorically perfect gases with unity values of molecular and turbulent Prandtl numbers. Major contributors to this discrepancy are the drainages of thermal energy primarily into vibrational excitation of N_2 and O_2, and secondarily into dissociation of O_2.
- The wall-normal location of the peak Favre-averaged temperature $y_{\widetilde{T},max}$ decreases monotonically with streamwise distance relative to δ^{99}. This trend is caused by the increase in Re_τ with distance downstream, which leads to an increasingly larger discrepancy between the thickness of the boundary layer and that of the viscous sublayer, the latter bearing the viscous stress responsible for aerodynamic heating by friction.
- Despite the high temperatures, the maximum turbulent Mach number $Ma_{t,max}$ reaches transonic values near the end of transition and remains high thereafter.

	Near resonance of 2D mode	Within secondary instability	Imminent breakdown to turbulence	Near end of transition	Turbulent	Turbulent
$\hat{x}$	400	700	1000	1300	1600	1750
$Re_x \times 10^{-6}$	2.79	4.64	6.59	8.44	10.3	11.2
Re_τ	140	160	197	529	961	1104
$Re_{\delta *} \times 10^{-4}$	4.89	5.69	3.05	3.49	3.50	4.28
Re_θ	535	792	1352	2032	3354	3826
$Ma_{t,max}$	0.31	0.25	0.44	1.04	0.82	0.80
$Da_{O_2} \times 10^2$	4.13	5.46	2.66	1.88	2.94	3.16
$\widetilde{T}_{max}/T_e$	4.12	4.10	3.99	3.77	4.07	4.06
$\widetilde{X}_{O,max}$	0.04	0.06	0.07	0.06	0.06	0.06
$\widetilde{X}_{NO,max}$	0.02	0.03	0.04	0.03	0.03	0.03
$y_{Ma_{t,max}}/\delta^{99}$	0.21	0.57	0.36	0.10	0.06	0.05
$y_{\lvert\dot{w}\rvert,O_2,max}/\delta^{99}$	0.19	0.55	0.42	0.04	0.02	0.02
$y_{\widetilde{T},max}/\delta^{99}$	0.36	0.35	0.26	0.10	0.04	0.03
$y_{\widetilde{X},O,max}/\delta^{99}$	0.18	0.19	0.13	0.02	0.01	0.01
$y_{\widetilde{X},NO,max}/\delta^{99}$	0.17	0.19	0.12	0.02	0.01	0.01
$\delta_{Ma_t}/\delta^{99}$	0.62	0.89	0.87	0.73	0.84	0.80
$\delta_{\widetilde{T}}/\delta^{99}$	0.71	0.68	0.65	0.53	0.38	0.38
δ_{O_2}/δ^{99}	0.34	0.30	0.27	0.28	0.09	0.08

TABLE 1. Time- and spanwise-averaged dimensionless quantities computed at the dimensionless streamwise locations indicated in the first row. In the notation, $\hat{x} = (x - x_o)/\delta_o^\star$ is the streamwise coordinate measured from the inlet domain location x_o and nondimensionalized with the displacement thickness of the inflow boundary layer $\delta_o^\star$; $Re_x = \rho_e U_e x/\mu_e$ is the Reynolds number based on the edge (post-shock) density ρ_e, velocity U_e, and viscosity μ_e; $Re_\tau = \overline{\rho_w} u_\tau \delta^{99}/\overline{\mu_w}$ is the friction Reynolds number based on the friction velocity $u_\tau = \sqrt{\overline{\tau_w}/\overline{\rho_w}}$, the mean wall density $\overline{\rho_w}$ and viscosity $\overline{\mu_w}$, and the local displacement thickness $\delta^\star$; $Re_{\delta^*} = \rho_e U_e \delta^*/\mu_e$ is the Reynolds number based on edge (post-shock) quantities; $Ma_{t,max} = \max(\sqrt{\overline{\boldsymbol{u}' \cdot \boldsymbol{u}'}}/\overline{a})$ is the maximum of the turbulent Mach number based on the fluctuations of the velocity vector $\boldsymbol{u}'$ and on the mean value of the local frozen speed of sound $\overline{a}$; $Da_{O_2} = (\lvert\overline{\dot{w}}_{O_2}\rvert/\overline{\rho})_{max}\delta^\star/u_\tau$ is the Damköhler number corresponding to the maximum mean dissociation rate of O_2; $\widetilde{T}_{max}/T_e$ represents the maximum of the Favre-mean static temperature divided by the edge (post-shock) temperature T_e; $y_{Ma_{t,max}}/\delta^{99}$, $y_{\widetilde{T},max}/\delta^{99}$, $y_{O_2,max}/\delta^{99}$, $y_{\widetilde{X},O,max}/\delta^{99}$, and $y_{\widetilde{X},NO,max}/\delta^{99}$ are, respectively, the nondimensional wall-normal locations of the maximum value of the turbulent Mach number, Favre-averaged temperature, the absolute mean dissociation rate of O_2, and the Favre-averaged molar fractions of O and NO; last, $\delta_{Ma_t}/\delta^{99}$, $\delta_{\widetilde{T}}/\delta^{99}$ and δ_{O_2}/δ^{99} are, respectively, the nondimensional thicknesses of the peaks of turbulent Mach number, Favre-averaged static temperature, and the absolute mean dissociation rate of O_2, which are defined as the difference of wall-normal locations where the local values are 50% of the peak value.

- The wall-normal location of the maximum turbulent Mach number $y_{Ma_{t,max}}$ evolves nonmonotonically with streamwise distance relative to δ^{99}, and is farthest from the wall during the growth of the secondary instability.
- The O_2-dissociation Damköhler number Da_{O_2} increases during the growth of the secondary instability, decreases upon breakdown, and increases again thereafter. However, the resulting values are small everywhere, and are representative of chemical nonequilibrium conditions.
- The Favre-averaged molar fractions of O and NO are maximum near the beginning

of the breakdown to turbulence, and decay thereafter to become mostly constant in the turbulent portion of the boundary layer, where $\widetilde{X}_{O,max} = 0.06$ and $\widetilde{X}_{NO,max} = 0.03$.

- The wall-normal locations of the maximum turbulent Mach number $y_{Ma_{t,max}}$, the mean temperature peak $y_{\widetilde{T},max}$, and the maximum mean rate of O_2 dissociation $y_{O_2,max}$, are all close to each other. These three maxima are located near the buffer zone at $y^\star \approx 10 - 20$ in semi-local inner units in the turbulent portion of the boundary layer, or equivalently, at distances of order $\delta^{99}/20 - \delta^{99}/50$ away from the wall.
- The wall-normal locations of the maximum molar fractions of O and NO, $y_{\widetilde{X},O,max}$ and $y_{\widetilde{X},NO,max}$, decrease relative to δ^{99} upon breakdown to turbulence. Thereafter, these two maxima become very close to the wall in the viscous sublayer, into which the dissociation products accumulate by molecular diffusion.
- In the turbulent portion of the boundary layer, the characteristic width of the wall-normal distribution of turbulent Mach number δ_{Ma_t} is much larger than the thickness of the aerodynamic-heating layer $\delta_{\widetilde{T}}$, and $\delta_{\widetilde{T}}$ is much larger than the characteristic thickness of the O_2-dissociation layer δ_{O_2} because of the high activation energy involved in the dissociation reaction. In particular, the approximate value of δ_{O_2} near the exit is about 100 semi-local inner units, or equivalently, 10% of δ^{99}.
- Much thinner than the dissociation-layer thickness δ_{O_2} (by a factor of 100) is the thickness of the recombination layer adjacent to the wall in $0 \leq y^\star \leq 1$, as depicted in Figure 3. In the present conditions, the heat released in the recombination layer is approximately 0.1% of the heat flux entering the wall and therefore is not critical in determining the thermal load on the airframe. However, if the surface material were catalytic or, as in carbon-fiber-reinforced silicon-carbide-based materials (C/C-SiC), became catalytic upon active oxidation at high temperatures, the recombination of O and N inside the wall could become an important source of internal structural heating.

It is worth underscoring that the scaling of the aformentioned results with the Mach number in hypersonic turbulent boundary layers at high enthalpies remains unknown.

3.3. *Turbulent fluctuations of the aerothermochemical field*

Figure 5 shows schematics of the distributions of the rms fluctuations of temperature and molar fractions, along with the streawmise and wall-normal Reynolds stresses in the turbulent portion of the boundary layer. Quantitative results can be found in Figures 4, 5, and 9 in Di Renzo & Urzay (2021). The following observations are worth highlighting:

- The wall-normal Reynolds stress $\overline{\rho}\widetilde{v''^2}$ peaks at a distance $y^\star \simeq 100$ away from the wall with a magnitude of approximately $1.2\overline{\tau_w}$.
- The tangential Reynolds stress $\overline{\rho}\widetilde{u''v''}$ is negative and attains a peak value of approximately $-1.2\overline{\tau_w}$ in the log layer, very close to the peak of $\overline{\rho}\widetilde{v''^2}$.
- The peak of the streamwise Reynolds stress $\overline{\rho}\widetilde{u''^2}$ is very close to the peak of the mean temperature at $y^\star \simeq 10$ and has a magnitude of approximately $12\overline{\tau_w}$.
- The peak of the rms of the temperature fluctuations $\sqrt{\widetilde{T''^2}}$ also occurs very close to $y^\star \simeq 10$ and has a magnitude of approximately $0.73T_e = 758$ K.
- The peak of the rms of the density fluctuations $\sqrt{\overline{\rho'^2}}$ occurs in the outer layer at $y^\star \simeq 1000$ and has a magnitude of approximately $0.21\rho_e = 0.04$ kg/m^3. This value, and that of the density variation across the nose shock, may be of relevance for estimating aero-optical distortions of electromagnetic waves captured by or emitted from the fuselage.
- The rms of the molar fractions are nonzero at the wall and peak at $y^\star \simeq 100$ away from it. For N_2 and O_2, this peak corresponds to a small percentage of approximately

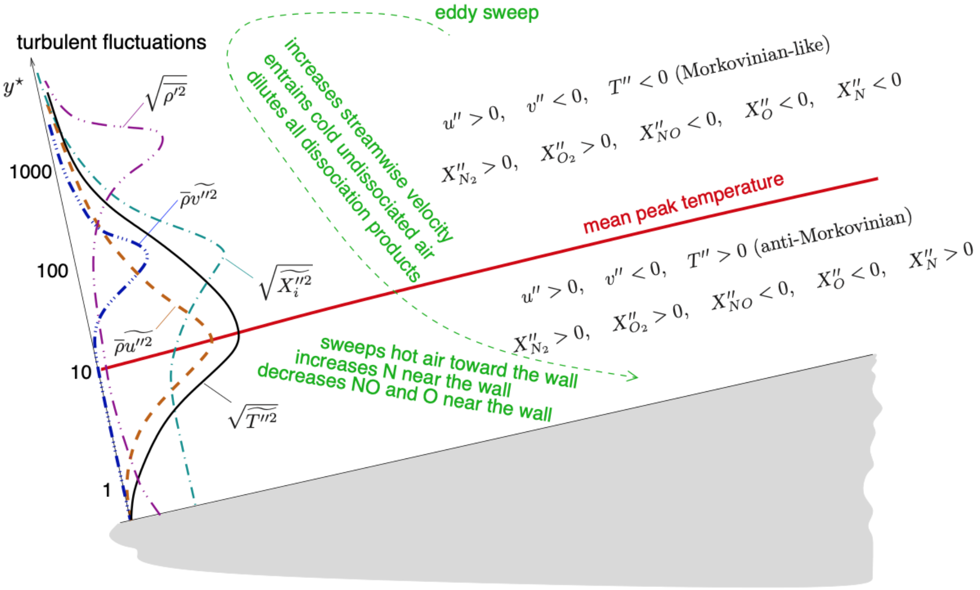
turbulent fluctuations
$y^\star$
1000
100
10
1
$\sqrt{\rho'^2}$
$\overline{\rho}\widetilde{v''^2}$
$\sqrt{\widetilde{X_i''^2}}$
$\overline{\rho}\widetilde{u''^2}$
$\sqrt{\widetilde{T''^2}}$
eddy sweep
increases streamwise velocity
entrains cold undissociated air
dilutes all dissociation products
$u'' > 0, \quad v'' < 0, \quad T'' < 0$ (Morkovinian-like)
$X''_{N_2} > 0, \quad X''_{O_2} > 0, \quad X''_{NO} < 0, \quad X''_{O} < 0, \quad X''_{N} < 0$
mean peak temperature
$u'' > 0, \quad v'' < 0, \quad T'' > 0$ (anti-Morkovinian)
$X''_{N_2} > 0, \quad X''_{O_2} > 0, \quad X''_{NO} < 0, \quad X''_{O} < 0, \quad X''_{N} > 0$
sweeps hot air toward the wall
increases N near the wall
decreases NO and O near the wall

FIGURE 5. Schematics of the turbulent fluctuations across the hypersonic boundary layer, including the signs of the disturbances associated with a sweep above and below the wall-normal location of the mean temperature peak.

1% of the local values of $\widetilde{X}_{N_2}$ and $\widetilde{X}_{O_2}$. In contrast, for O and NO, much larger rms fluctuations of 25% of the local values of $\widetilde{X}_O$ and $\widetilde{X}_{NO}$ are observed.

As illustrated in Figure 5, in the log and outer regions of the boundary layer, where the mean temperature decreases from $\widetilde{T}_{max}$ to the edge value T_e, large eddies sweeping into the boundary layer lead to $u'' > 0$, $v'' < 0$, $T'' < 0$, $X''_{N_2} > 0$, and $X''_{O_2} > 0$ by entraining faster and colder undissociated air from the edge of the boundary layer. In the buffer zone and viscous sublayer, where the mean temperature decreases from $\widetilde{T}_{max}$ to the wall value, this entrainment leads to $u'' > 0$, $v'' < 0$, $T'' > 0$, $X''_{N_2} > 0$, $X''_{O_2} > 0$, and to a positive fluctuation of atomic nitrogen $X''_N > 0$ because of the bell-shaped concentration distribution of $\widetilde{X}_N$ resulting from the quasi-steady state of N, as further explained in Di Renzo & Urzay (2021). The opposite trends in fluctuations hold for ejections.

3.4. *The unclosed turbulent fluctuations of the chemical production rates*

In modeling endeavors for hypersonic turbulent flows, it is convenient to consider the unclosed quantity

$$\dot{w}_i^I = \overline{\dot{w}}_i - \dot{w}_i(\widetilde{T}, \overline{P}, \widetilde{X}_{j|j=1,\dots,N_s}), \tag{3.1}$$

which represents the fluctuations of the chemical production rate of species i with respect to that based on the mean values of temperature, pressure, and composition, with N_s denoting the number of species (Duan & Martin 2011*b*). Although $\dot{w}_i^I$ does not account for the full fluctuations of the chemical production rate, it is a relevant quantity for a-priori quantification of the relative importance of SGS modeling of turbulence-thermochemistry interactions in numerical simulations. Since only the mean (or filtered) aerothermochemical variables are available in RANS (or LES) of turbulent hypersonic flows (see Appendix), $\overline{\dot{w}_i}$ has to be closed either with an SGS model or with the simplest

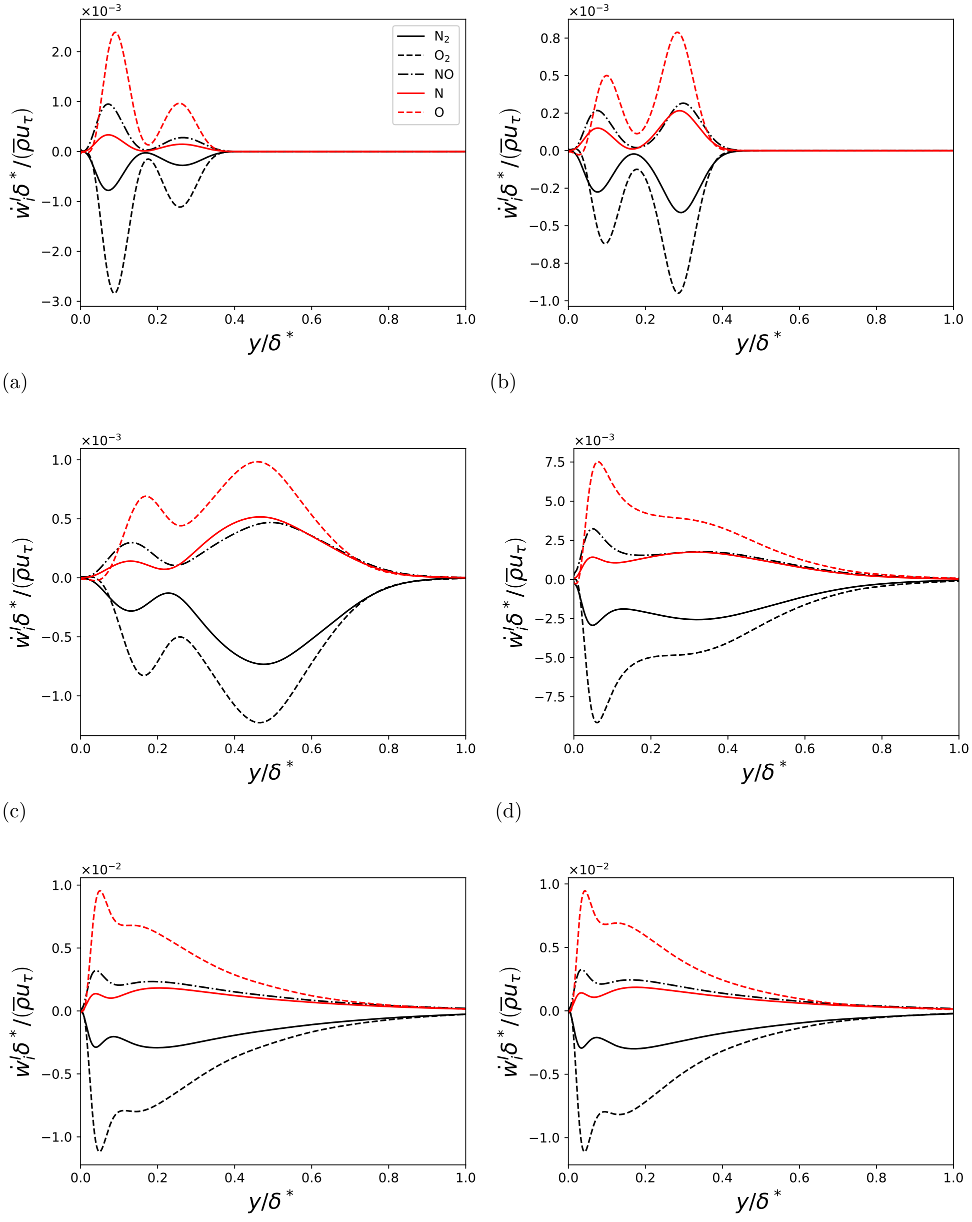

(a) (b) (c) (d) (e) (f)

FIGURE 6. Wall-normal profiles of $\dot{w}_i^I$ in inner semi-local units at (a) $\hat{x} = 400$: near resonance of the second mode; (b) $\hat{x} = 700$: within the stage of growth of the secondary instability; (c) $\hat{x} = 1000$: near imminent breakdown to turbulence; (d) $\hat{x} = 1300$: near the end of transition; (e) $\hat{x} = 1600$ and (f) 1750: both in the turbulent boundary layer.

approximation

$$\overline{\dot{w}_i} \approx \dot{w}_i(\widetilde{T}, \overline{P}, \widetilde{X}_{j|j=1,\ldots,N_s}). \tag{3.2}$$

The latter corresponds to neglecting $\dot{w}_i^I$, or equivalently, to neglecting SGS turbulence-thermochemistry interactions.

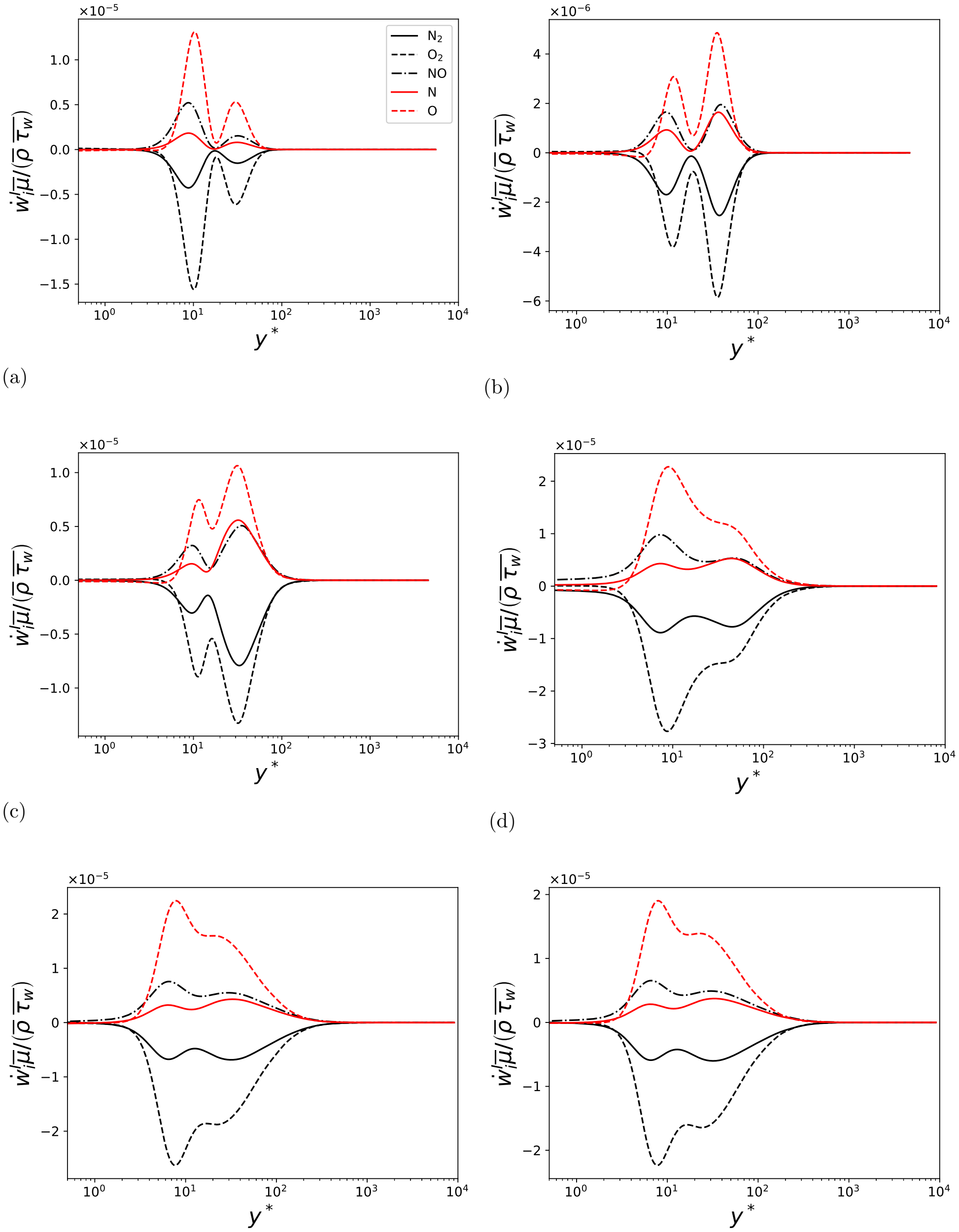

(a)

(b)

(c)

(d)

(e)

(f)

FIGURE 7. Wall-normal profiles of $\dot{w}_i^I$ in inner semi-local units. The panels in this figure correspond to the same streamwise locations as those indicated in the caption of Figure 6.

The wall-normal distributions of $\dot{w}_i^I$ in outer and semi-local inner units are shown in Figures 6 and 7, respectively. The breakdown to turbulence increases the magnitude of $\dot{w}_i^I$, widens their distributions, and shifts the wall-normal location of their absolute maximum values toward the wall in outer units, with $\dot{w}_{O_2}^I$ and $\dot{w}_O^I$ being the two largest rates. The largest values of $\dot{w}_i^I$ in the turbulent portion of the boundary layer lie in the buffer zone, near the mean temperature peak.

A comparison between Figure 6 in this report and Figure 7 in Di Renzo & Urzay (2021) indicates that the peak values of $\dot{w}_i^I$ are approximately 10%-20% of those of the mean rates $\overline{\dot{w}_i}$ of N_2, O_2, NO, and O. In contrast, the magnitude of $\dot{w}_N^I$ is comparable to that of $\overline{\dot{w}_N}$. In principle, the approximation (3.2) may therefore be worse for N than for the rest of the species. Nonetheless, the maximum value of the Favre-averaged molar fraction of atomic nitrogen, $\widetilde{X}_N = 2.6\cdot 10^{-4}$, is small and therefore largely inconsequential in the present operating conditions. As a result, the approximation (3.2) for O_2 and O could be much more detrimental for predictions despite the fact that SGS turbulence-thermochemistry interactions are weaker for these species than for N (Duan & Martin 2011*b*). However, a-posteriori analyses of RANS or LES results would be required for a corroboration of these statements.

The SGS modeling of chemical reaction rates in RANS or LES of hypersonic turbulent flows at high enthalpies remains an open problem. Some progress in this area could perhaps be enabled by multiscale modeling strategies borrowed from computational high-speed turbulent combustion (Peters 2000; Pierce & Moin 2004; Urzay 2018).

3.5. *Influences of variations of geometry and operating conditions on the coupling between turbulence and thermochemical effects*

Figure 8(b-g) summarizes six variants of the reference configuration in panel (a). The first four variants decrease the coupling between turbulence and thermochemical effects:

- In Figure 8(b), an increase in the wedge angle leads to an increase in the post-shock temperature and mean peak temperature in the boundary layer, along with a decrease in the post-shock unit Reynolds number and edge Mach number. Larger concentrations of O and NO both in the boundary layer and in the overriding inviscid hot shock layer occur because of the high temperatures. However, the lower Reynolds number of the boundary layer tends to delay transition and suppress turbulence.
- In Figure 8(c), a decrease in the wedge angle leads to a decrease in the post-shock temperature and in the mean peak temperature in the boundary layer, along with an increase in the post-shock unit Reynolds number and the edge Mach number. The lower temperatures suppress air dissociation, but the higher Reynolds number of the boundary layer advances transition and intensifies turbulence. However, the increase in post-shock unit Reynolds number with decreasing wedge angle is not monotonic, as discussed below.
- In Figure 8(d), the modification of the wedge shown in Figure 8(b) into a blunt body generates a strong bow shock that, close to the axis, leaves very hot subsonic air downstream. As a result, the post-shock Reynolds number and edge Mach number are much smaller than those in the reference configuration. The air downstream of the bow shock is highly dissociated in O, NO, and N, but remains mostly laminar because of the low Reynolds number of the boundary layer and the favorable pressure gradient induced by the convex curvature. Turbulence in the boundary layer is largely impaired by the small Reynolds number and may appear only far away from the axis.
- In Figure 8(e), a further decrease in the wedge angle, down to values comparable to the Mach angle, transforms the nose shock into a Mach wave across which the temperature, unit Reynolds number, and Mach number remain mostly constant. As a result, the post-shock air is cold, undissociated, and low pressure. Since the normal Mach number is close to unity, the inviscid portion of the flow can be characterized not as hypersonic but as linearly supersonic (Urzay 2020). Nonetheless, the ensuing boundary layer is driven hypersonically by the highest-possible edge Mach number, namely that of the free stream.

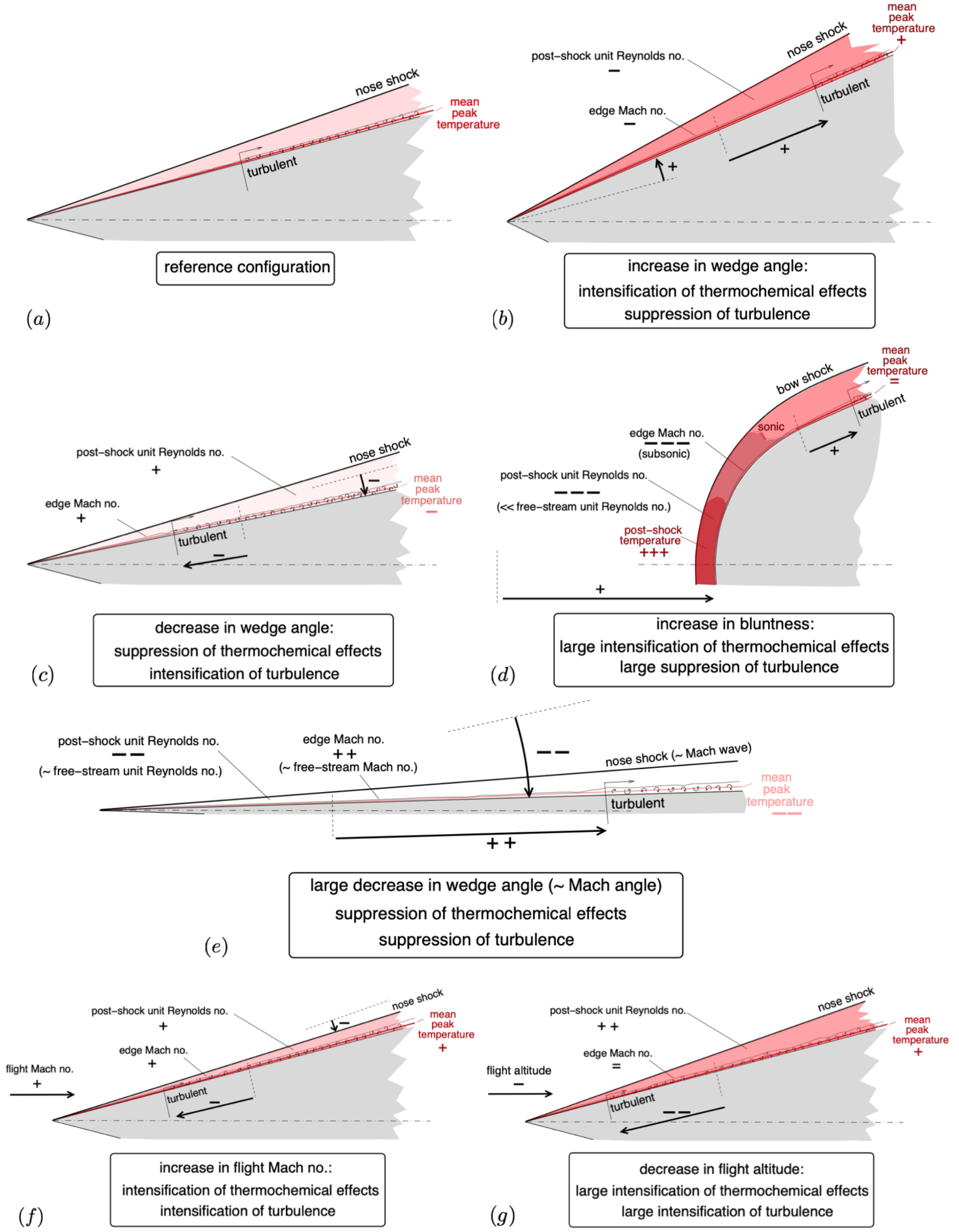
nose shock
mean
peak
temperature
turbulent
reference configuration
(a)
post–shock unit Reynolds no.
−
nose shock
mean
peak
temperature
+
edge Mach no.
−
turbulent
+
+
increase in wedge angle:
intensification of thermochemical effects
suppression of turbulence
(b)
post–shock unit Reynolds no.
+
nose shock
−
mean
peak
temperature
−
edge Mach no.
+
turbulent
−
decrease in wedge angle:
suppression of thermochemical effects
intensification of turbulence
(c)
mean
peak
temperature
=
bow shock
turbulent
sonic
edge Mach no.
− − −
(subsonic)
+
post–shock unit Reynolds no.
− − −
(<< free–stream unit Reynolds no.)
post–shock
temperature
+++
+
increase in bluntness:
large intensification of thermochemical effects
large suppression of turbulence
(d)
post–shock unit Reynolds no.
− −
(~ free–stream unit Reynolds no.)
edge Mach no.
+ +
(~ free–stream Mach no.)
− −
nose shock (~ Mach wave)
mean
peak
temperature
− −
turbulent
+ +
large decrease in wedge angle (~ Mach angle)
suppression of thermochemical effects
suppression of turbulence
(e)
post–shock unit Reynolds no.
+
nose shock
−
mean
peak
temperature
+
edge Mach no.
+
flight Mach no.
+
turbulent
−
increase in flight Mach no.:
intensification of thermochemical effects
intensification of turbulence
(f)
post–shock unit Reynolds no.
+ +
nose shock
mean
peak
temperature
+
edge Mach no.
=
flight altitude
−
turbulent
− −
decrease in flight altitude:
large intensification of thermochemical effects
large intensification of turbulence
(g)

FIGURE 8. Qualitative influences of variations of the geometry and operating conditions of the reference configuration on turbulence and thermochemical effects.

Despite the higher edge Mach number, the mean peak temperature in the boundary layer is smaller than that in the reference configuration, thereby leading to smaller concentrations of dissociation products everywhere. In addition, the lower Reynolds number of the resulting boundary layer delays transition and suppresses turbulence.

In contrast, the last two variants in Figure 8 increase the coupling between turbulence and thermochemical effects:

- In Figure 8(f), an increase in the flight Mach number leads to higher values of the edge Mach number, post-shock unit Reynolds number, post-shock temperature, and mean peak temperature in the boundary layer. As a result, in comparison with the reference configuration, the concentration of air dissociation products is larger in both the boundary layer and the inviscid hot shock layer. In addition, the higher Reynolds number of the boundary layer advances transition and intensifies turbulence.
- In Figure 8(g), a decrease in the flight altitude increases the post-shock unit Reynolds number and post-shock temperature, the latter inducing a larger peak value of the mean temperature in the boundary layer. The consequences are similar to those of increasing the flight Mach number, in that both turbulence and thermochemical effects are intensified. However, the inverse exponential dependence of density on altitude makes small negative variations in altitude to engender a very large increase in the Reynolds number of the boundary layer. For instance, had the Mach-23 reference configuration been operating at sea level, its post-shock unit Reynolds number would have been of order 10^9 m^{-1}. Remarkably, in those conditions, the post-shock pressure would be approximately 40 bar, thereby yielding post-shock air in supercritical state, a thermodynamic effect that has rarely, if ever, been considered in fundamental studies of hypersonic flows.

These considerations highlight leading-order effects that the flight altitude, flight Mach number, and particular design of the forebody geometry of the hypersonic flight system may have on the character of the ensuing post-shock flow from the perspective of potentially sustaining turbulence in the boundary layers enveloping the fuselage. In considering these effects, it is important to note that, in practical applications, variations in geometry (by erosion, deformation, or charring of the fuselage, or by variable-geometry surfaces) and operating conditions (by changes in altitude and velocity) may occur simultaneously and dynamically in real hypersonic flight systems during their trajectory.

4. Thermodynamic-nonequilibrium effects

In the analysis above, the air around the wedge is assumed to be in vibrational equilibrium, in that the internal energy of the vibrational degrees of freedom relaxes infinitely fast to its equilibrium value. The incorporation of thermodynamic nonequilibrium effects on hypersonic turbulent boundary layers, much of which remains unexplored in the scientific literature, complicates the description. The discussion here is therefore solely based on intuition and first principles, and its corroboration may be the subject of future work.

4.1. *Vibrational relaxation in the shock layer*

In the reference configuration shown in Figure 2, the moderate post-shock temperature $T_e = 1039$ K renders exceedingly long vibrational-relaxation times t_v [see page 58 in Park (1990) for details of the calculation of t_v]. However, the contribution of the vibrational degrees of freedom to the internal energy at this temperature is small (7% for N_2 and 16% for O_2). As a result, the approximation of vibrational equilibrium in calculating the specific heats and internal energy of the gas in the shock layer has a negligible effect.

A vibrational-relaxation layer would emerge immediately downstream of the nose shock in cases in which the post-shock temperature may be sufficiently high to yield an order-unity ratio between the vibrational internal energy and the sum of translational and rotational internal energies (i.e., $T_e \gtrsim 2500 - 3000$ K). In this layer, the vibrational temperature would lag behind the translational temperature after the latter increases

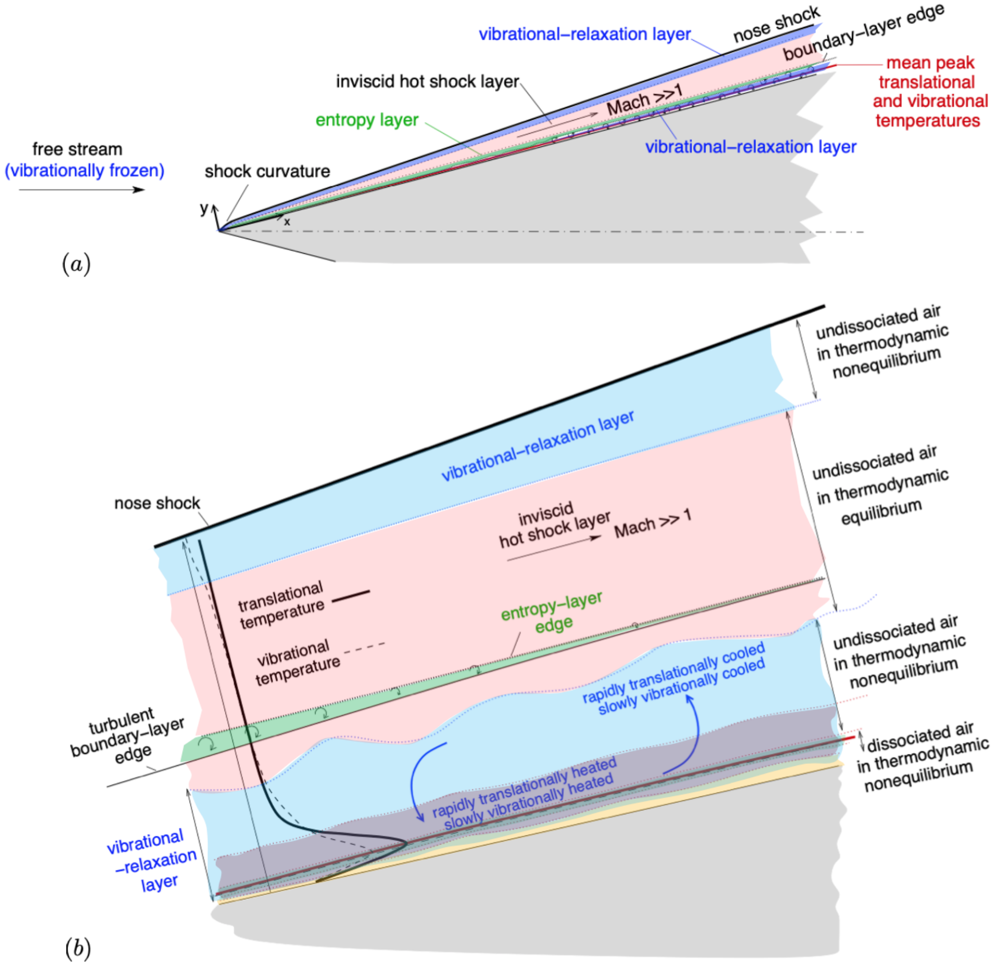
vibrational–relaxation layer
nose shock
boundary–layer edge
inviscid hot shock layer
mean peak translational and vibrational temperatures
entropy layer
Mach >>1
vibrational–relaxation layer
free stream
(vibrationally frozen)
shock curvature
y
x
(a)
undissociated air in thermodynamic nonequilibrium
vibrational–relaxation layer
undissociated air in thermodynamic equilibrium
nose shock
inviscid hot shock layer
Mach >> 1
translational temperature
vibrational temperature
entropy–layer edge
undissociated air in thermodynamic nonequilibrium
rapidly translationally cooled
slowly vibrationally cooled
turbulent boundary–layer edge
rapidly translationally heated
slowly vibrationally heated
dissociated air in thermodynamic nonequilibrium
vibrational –relaxation layer
(b)

FIGURE 9. Schematics of thermodynamic nonequilibrium effects.

rapidly across the nose shock, as sketched in Figure 9. The thickness of this layer would be of the same order as the post-shock normal velocity multiplied by the local vibrational-relaxation time t_v.

4.2. *Vibrational relaxation in the boundary layer*

The high temperatures induced by aerodynamic heating profusely activate the vibrational degrees of freedom in the boundary layer. Near the peak temperature, the local values of the characteristic vibrational relaxation time scale t_v for N_2 and O_2 are, respectively, 12 times and 1.4 times larger than the residence time $x_o/U_e = 2.1$ μs of the gas within the laminar boundary layer at $x = x_o$. As a result, the N_2 in the boundary layer entering the computational domain should not be assumed to be in vibrational equilibrium.

Farther downstream, near the exit of the computational domain at $x = x_1$, the residence time of the gas molecules based on their mean motion in the turbulent boundary layer has increased to $x_1/U_e = 62$ μs, or equivalently, to $2.5t_v$ and $21t_v$ for for N_2 and O_2, respectively. This indicates that the mean motion through the boundary layer is sufficiently slow to allow for vibrational relaxation of O_2 and – to a lesser extent – N_2.

Nonetheless, the air would still remain away from vibrational equilibrium in the hypersonic turbulent boundary layer because of a nonequilibrium effect by the velocity fluctuations on the mean translational and vibrational temperatures, as described below.

An additional complexity introduced by turbulent motion in the boundary layer is that the large-scale eddies continuously mix air near the outer edge of the boundary layer at $T_e = 1039$ K with hot air in the aerodynamic-heating layer at $\widetilde{T}_{max} = 4220$ K. As indicated in Figure 9, this stirring motion would induce a vibrational-relaxation layer whose thickness would be of the same order as $u_\tau t_v$. A vibrational turbulent Damköhler number $Da_v = \delta^\star/(u_\tau t_v)$ quantifies the ratio between the thicknesses of the boundary layer and the vibrational-relaxation layer within, with $Da_v = O(1)$ being the dynamically relevant regime. Inside the vibrational-relaxation layer, the vibrational temperature would lag behind the translational temperature near its mean peak value, but would lead in the outer layer instead. To see this, notice that, near the mean temperature peak, sweeps would bring colder air from the outer layer that would rapidly equilibrate translationally with the hot air beneath because of heat conduction, whereas the vibrational equilibration would be slower. The opposite trend would hold for ejections.

At $x = x_1$, the turnover time of the large-scale eddies is $\delta_1^\star/u_\tau = 19$ μs, which is slower than t_v by a factor of 13 for O_2, but faster than t_v by a factor of 1.3 for N_2, with t_v based on $\widetilde{T}_{max}$ in these conservative estimates. In this way, whereas the O_2 molecules would vibrationally equilibrate within a distance of $u_\tau t_v = \delta_1^\star/13$ when overturned by these large eddies, the N_2 molecules would remain vibrationally frozen (during sweeps) or vibrationally equilibrated (during ejections).

The dissociation of N_2 in the present conditions is negligible, and therefore the effect of the vibrational nonequilibrium of the N_2 molecules is restricted to modifying the thermal inertia of the gas through the calculation of its specific heat and internal energy. By contrast, the approximation of vibrational equilibrium for O_2 molecules may overestimate its rate of dissociation, since the latter scales with the exponential of the geometric average of the translational and vibrational temperatures (Park 1989).

Near the wedge vertex, thermodynamic noequilibrium induces a shock curvature of the same order as the inverse of the multiplication of the normal post-shock velocity and t_v evaluated with post-shock conditions. This curvature produces a favorable local pressure gradient and an entropy layer of stabilizing vorticity that overrides the boundary layer. These two phenomena are clearly unfavorable for the onset of turbulence but complicate the overall description of the boundary layer.

4.3. *A comment on conditions leading to thermodynamic nonequilibrium*

Despite the towering inferno that in principle the problem of hypersonic turbulent boundary layers may become upon incorporating these additional complexities, there is hope for progress because of the following reason. Vibrational nonequilibrium effects become increasingly less important at increasingly lower altitudes and increasingly higher velocities, both of which represent trends promoting turbulence, as discussed in Section 3.5. Specifically, the lower the altitude is, the larger the air density is, and the more frequent molecular collisions are, thereby decreasing t_v. Similarly, the higher the flight speed is, the larger the post-shock temperature and the mean peak temperature in the boundary layer are, thereby decreasing t_v as well. Because of the exponential dependence of t_v on temperature, and the quadratic dependence of temperature on flight speed, the decrease in t_v occurring upon increasing the flight speed would probably outplay the decrease in residence time induced by increasingly higher flight speeds, thereby shrinking all regions of the flow dominated by vibrational nonequilibrium. However, all the considerations above are open research questions that would greatly benefit from fundamental investigations. The wall-modeled LES formulation provided in the Appendix could help to alleviate the computational cost of exploratory numerical simulations.

5. Concluding remarks

In concluding this report, it is not our desire to restate here the results that have already been summarized above, or the open questions that have been deliberately placed at the end of each section. Instead, let us remark the wealth of phenomena that emerges in hypersonic flows at high enthalpies and high Reynolds numbers. Turbulence prevails at low altitudes in hypersonic boundary layers at suborbital enthalpies, and its dynamics are largely unknown. A number of characteristic scales are introduced by compressibility and thermochemical nonequilibrium that complicate the description. In addition, different combinations of flight operating conditions make some physical processes dominate over others. This large space of parameters is in contrast to that in incompressible turbulent boundary layers, where the solution depends, at most, on the Reynolds number, and to that in compressible turbulent boundary layers of calorically perfect gases, where the solution depends, at most, on the adiabatic coefficient, the wall-to-stagnation temperature ratio, the Reynolds number, and the Mach number.

The Mach-number trends shown in Figure 10 indicate that the field of hypersonics continues to flourish long after the exponential pace of research that led to the ICBM and Apollo programs from the 1950's until the early 1970's. Other technological advances not shown in Figure 10, which will significantly challenge the state of the art of hypersonic flight engineering in the short term, will be the upcoming Mars Sample Return mission and an eventual manned mission to Mars. These space missions will have to address, for the first time, the problem of multiplanetary hypersonic flight as a double entry in two very different atmospheres: first entering and navigating the martian atmosphere in the outbound flight, and then re-entering the terrestrial atmosphere in the return voyage. The physical characteristics of the hypersonic flow around the spacecraft in those two legs of the journey will also be quite different. All this astounding progress in applied aspects of hypersonics, and the variety of flow regimes it involves, would benefit from a closer fundamental understanding of the interactions of turbulence with thermochemical effects at hypersonic velocities – a problem that remains unchallenged.

Acknowledgments

The first author acknowledges funding from the Hypersonic Aerothermodynamics portfolio of the U.S. Air Force Office of Scientific Research (AFOSR), grant # FA9550-16-1-0319, and from the Advanced Simulation and Computing (ASC) program of the U.S. Department of Energy's National Nuclear Security Administration (NNSA) via the PSAAP-II Center at Stanford, grant # DE-NA0002373. The second author acknowledges funding from the European Union's Horizon 2020 Research and Innovation Programme under the Marie S. Curie grant # 898458.

Appendix. Wall-modeled LES formulation for hypersonic turbulent flows in thermochemical nonequilibrium

In this Appendix, the Favre-filtered value of any variable f is denoted $\widetilde{f}$, with f'' as the corresponding fluctuation. The symbols $\overline{f}$ and f' represent, respectively, the Reynolds-filtered value and its corresponding fluctuation. The two-temperature approach of Park

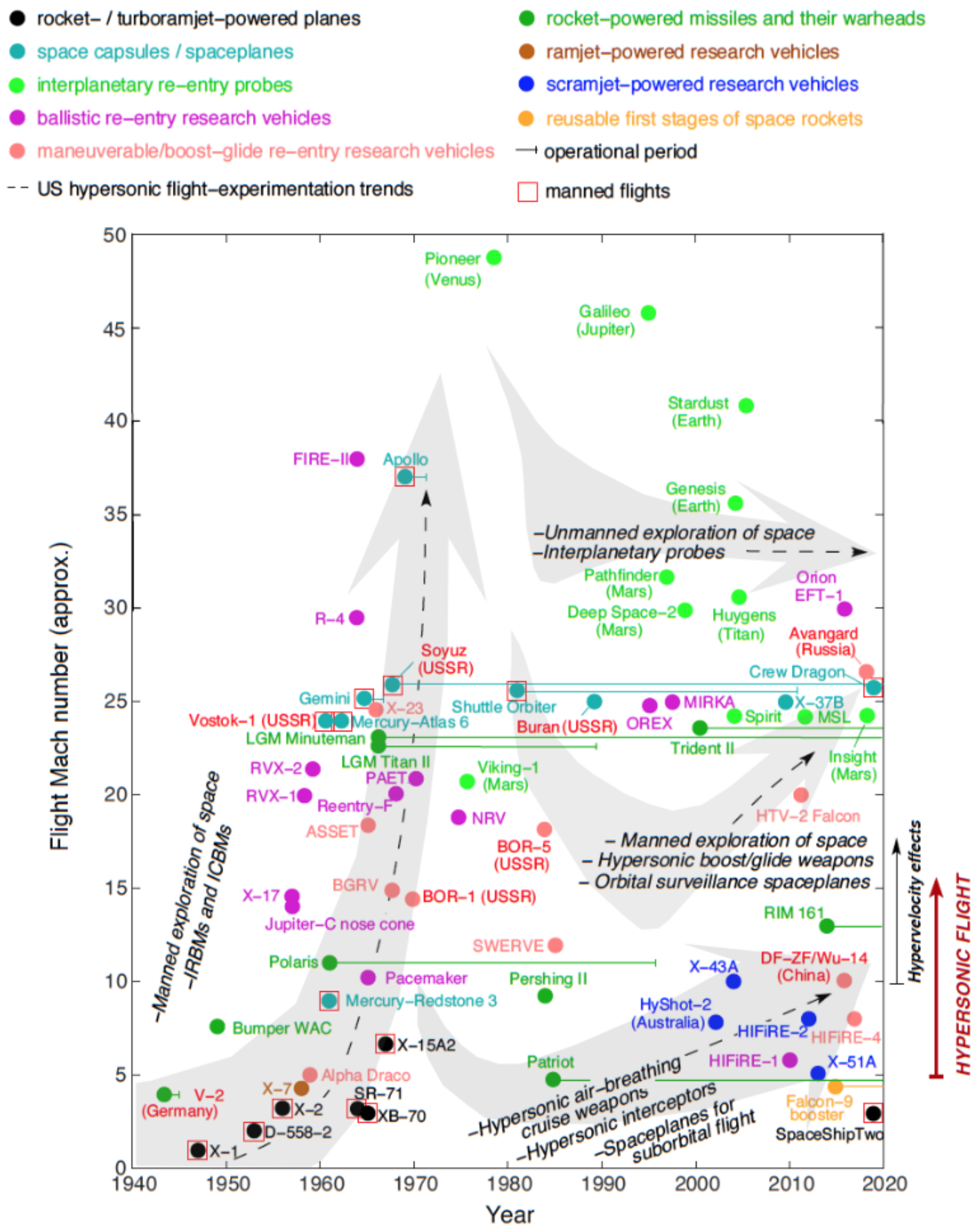

FIGURE 10. Historical evolution of the flight Mach number of several US high-speed aerospace systems during the years 1940-2020 collected from publicly available literature. Also included are relevant foreign hypersonic flight systems from USSR/Russia, China, Germany, and Australia. Excluded are programs cancelled before flight testing. The dashed lines indicate trends in US hypersonic flight experimentation.

(1990) is used that treats separately the translational-rotational temperature T and the vibrational temperature T_v.

A.1. *Conservation equations for the resolved LES field*

The LES equations of conservation of mass, momentum, species, vibrational internal energy, and static enthalpy are given by

$$\frac{\partial \overline{\rho}}{\partial t} + \nabla \cdot (\overline{\rho} \widetilde{\boldsymbol{u}}) = 0, \tag{A 1}$$

$$\frac{\partial}{\partial t}(\overline{\rho} \widetilde{\boldsymbol{u}}) + \nabla \cdot (\overline{\rho} \widetilde{\boldsymbol{u}} \widetilde{\boldsymbol{u}}) = -\nabla \overline{P} + \nabla \cdot \overline{\boldsymbol{\tau}} - \nabla \cdot \boldsymbol{\mathcal{T}}, \tag{A 2}$$

$$\frac{\partial}{\partial t}(\overline{\rho} \widetilde{Y}_i) + \nabla \cdot (\overline{\rho} \widetilde{\boldsymbol{u}} \widetilde{Y}_i) = -\nabla \cdot (\overline{\rho} \widetilde{\boldsymbol{V_i}} \widetilde{Y}_i) - \nabla \cdot \boldsymbol{\mathcal{J}_i} + \overline{\dot{w}_i}, \quad i = 1, 2 \ldots N_s, \tag{A 3}$$

$$\frac{\partial}{\partial t}(\overline{\rho} \widetilde{e}_v) + \nabla \cdot (\overline{\rho} \widetilde{\boldsymbol{u}} \widetilde{e}_v) = \nabla \cdot (\widetilde{\lambda}_v \nabla \widetilde{T}_v) - \nabla \cdot \boldsymbol{\mathcal{E}} + \overline{\dot{Q}}_{v-t}, \tag{A 4}$$

$$\frac{\partial}{\partial t}(\overline{\rho} \widetilde{h}) + \nabla \cdot (\overline{\rho} \widetilde{\boldsymbol{u}} \widetilde{h}) = \frac{\partial \overline{P}}{\partial t} + \widetilde{\boldsymbol{u}} \cdot \nabla \overline{P}$$
$$+ \nabla \cdot \left(\widetilde{\lambda} \nabla \widetilde{T} - \sum_{i=1}^{N_s} \overline{\rho} \widetilde{h}_i \widetilde{\boldsymbol{V_i}} \widetilde{Y}_i \right) - \nabla \cdot \boldsymbol{\mathcal{Q}} + \overline{\boldsymbol{\tau}} : \nabla \widetilde{\boldsymbol{u}} - \boldsymbol{\mathcal{T}} : \nabla \widetilde{\boldsymbol{u}}. \tag{A 5}$$

In this formulation, $\widetilde{\rho}$ is the filtered density, $\widetilde{\boldsymbol{u}}$ is the filtered velocity vector, and $\overline{\boldsymbol{\tau}}$ is the viscous stress tensor based on the gradients of the filtered velocities. Similarly, $\widetilde{\lambda}$ and $\widetilde{\lambda_v}$ are translational and vibrational filtered thermal conductivities [see Johnson & Candler (2005) for a method of calculation for λ_v]. Additionally, $\widetilde{Y}_i$, $\widetilde{\boldsymbol{V_i}}$, and $\overline{\dot{w}}_i$ are, respectively, the filtered mass fraction, the molecular diffusion velocity based on the filtered gradients of the mass and molar fractions, and the filtered chemical production rate of species i, with N_s being the number of species in the mixture [see Di Renzo & Urzay (2021) for definitions of $\boldsymbol{V_i}$ and $\dot{w}_i$]. At moderate post-shock pressures, Eqs. (A 1)-(A 5) are supplemented with the ideal-gas equation of state

$$\overline{P} = \overline{\rho} \widetilde{R}_g \widetilde{T}, \tag{A 6}$$

where $\widetilde{R}_g = \mathrm{R}^0 / \widetilde{W}$ is the filtered gas constant based on the universal gas constant R^0 and on the filtered mean molecular weight $\widetilde{W} = \sum_{i=1}^{N_s} (\widetilde{Y}_i / W_i)^{-1}$, with W_i being the molecular weight of species i.

The filtered static enthalpy $\widetilde{h}$ is the sum of filtered partial-specific enthalpies $\widetilde{h}_i$,

$$\widetilde{h} = \sum_{i=1}^{N_s} \widetilde{Y}_i \widetilde{h}_i = \sum_{i=1}^{N} \widetilde{Y}_i [h_i^0 + \widetilde{h}_{tr,i}(\widetilde{T}) + \widetilde{e}_{rot,i}(\widetilde{T}) + \widetilde{e}_{v,i}(\widetilde{T_v}) + \widetilde{e}_{el,i}(\widetilde{T})], \tag{A 7}$$

where h_i^0 is the formation enthalpy, $\widetilde{h}_{tr,i} = (5/2) R_{g,i} \widetilde{T}$ is the filtered partial-specific enthalpy of translational motion, $\widetilde{e}_{rot,i} = R_{g,i} \widetilde{T}$ is the filtered partial-specific internal energy of rotational motion, $\widetilde{e}_{v,i} = (\theta_{v,i} R_{g,i}) / [\exp(\theta_{v,i} / \widetilde{T}_v) - 1]$ is the filtered partial-specific internal energy of vibrational motion, and $\widetilde{e}_{el,i} = \sum_{k=1} r_{k,i} \exp(-\theta_{el,k,i} / \widetilde{T})$ is the filtered partial-specific internal energy of electronic excitation, which is assumed to be in equilibrium. Whereas $r_{k,i}$ are pre-exponential factors of the internal energy of electronic excitation, the quantities $R_{g,i}$, $\theta_{v,i}$, and $\theta_{el,k,i}$ represent, respectively, the gas constant and activation temperatures of vibration and electronic excitation of species i.

A.2. *Closures for subgrid-scale fluxes and source terms*

The symbol $\boldsymbol{\mathcal{T}} = \overline{\rho}(\widetilde{\boldsymbol{u}\boldsymbol{u}} - \widetilde{\boldsymbol{u}}\widetilde{\boldsymbol{u}})$ denotes the SGS stress, whereas $\boldsymbol{\mathcal{J}_i} = \overline{\rho}(\widetilde{\boldsymbol{u}Y_i} - \widetilde{\boldsymbol{u}}\widetilde{Y}_i)$, $\boldsymbol{\mathcal{E}} = \overline{\rho}(\widetilde{\boldsymbol{u}e_v} - \widetilde{\boldsymbol{u}}\widetilde{e}_v)$, and $\boldsymbol{\mathcal{Q}} = \overline{\rho}(\widetilde{\boldsymbol{u}h} - \widetilde{\boldsymbol{u}}\widetilde{h})$ are the SGS fluxes of species, vibrational internal energy, and static enthalpy, respectively. These quantities are closed using the Boussinesq approximation as

$$\boldsymbol{\mathcal{J}_i} = -\frac{\mu_t}{Sc_{t,i}}\nabla\widetilde{Y}_k, \quad \boldsymbol{\mathcal{E}} = -\frac{\mu_t}{Pr_{t,v}}\nabla\widetilde{e}_v, \quad \boldsymbol{\mathcal{Q}} = -\frac{\mu_t}{Pr_t}\nabla\widetilde{h},$$

$$\boldsymbol{\mathcal{T}} - \frac{2}{3}k_{sgs}\boldsymbol{I} = -2\mu_t\left(\boldsymbol{S} - \frac{\widetilde{\Delta_v}}{3}\boldsymbol{I}\right). \tag{A 8}$$

In these expressions, $\boldsymbol{S}$ is the strain-rate tensor, $\boldsymbol{I}$ is the identity tensor, $\widetilde{\Delta_v}$ is the resolved dilatation, μ_t is the eddy viscosity, and k_{sgs} is the SGS kinetic energy. In particular, μ_t and k_{sgs} can be obtained directly, for instance, by using the dynamic model of Moin *et al.* (1991). Similarly, $Sc_{t,i}$ Pr_t, and $Pr_{t,v}$ are the eddy Schmidt number of species i, the eddy Prandtl number, and the eddy vibrational Prandtl number. These three quantities can also be obtained dynamically by replacing $\widetilde{T}$ in Eq. (19) of Moin *et al.* (1991) with $\widetilde{Y}_i$ (for $Sc_{t,i}$), with $\widetilde{h}$ (for Pr_t), and with $\widetilde{e}_v$ (for $Pr_{t,v}$), where $\widetilde{e}_v = \sum_{i=1}^{N_s}\widetilde{Y}_i\widetilde{e}_{v,i}$ is the specific vibrational internal energy of the mixture.

Compared with the closures outlined above, the closures for the thermochemical source terms $\overline{\dot{w}}_i$ and $\overline{\dot{Q}}_{v-t}$ may be significantly more involved. In its simplest form, $\overline{\dot{w}}_i$ could be approximated using Eq. (3.2), as discussed in Section 3.4. However, the accuracy of such approximation represents an open research question. Similarly to Eq. (3.2), the source term $\overline{\dot{Q}}_{v-t}$, which represents the filtered rate of exchange of energy between translational-rotational and vibrational energies due to collisional processes, could be approximated, in the simplest way, by the Landau-Teller theory (Landau & Teller 1936), evaluated with filtered aerothermochemical quantities as

$$\overline{\dot{Q}}_{v-t} \approx \sum_{i=1}^{N_s}\overline{\rho}\widetilde{Y}_i\frac{\widetilde{e}_{v,i}^{eq}(\widetilde{T}) - \widetilde{e}_{v,i}(\widetilde{T}_v)}{t_{v,i}(\widetilde{T},\overline{P})}. \tag{A 9}$$

In Eq. (A 9), $\widetilde{e}_{v,i}^{eq}$ is the filtered partial-specific equilbrium internal energy of vibrational motion. Additionally, $t_{v,i}$ is a mass-averaged time scale for vibrational relaxation of species i by collisions with all other species, which is based on the filtered temperature and pressure. Whether Eq. (A 9) is a good approximation for turbulent flows, or more sophisticated closures are required that incorporate the effects of SGS fluctuations and their correlations, is also an open research question. Additional effects of dissociation on the depletion of vibrational energy, not included in Eq. (A 9), would also influence the filtered rate of energy exchange, which would then become an explicit function of the filtered chemical rates of molecular dissociation (Park 1990).

The relative effect of the thermochemical source terms $\overline{\dot{w}}_i$ and $\overline{\dot{Q}}_{v-t}$ on the LES conservation equations outlined above depends not only on the operating conditions but also on the choice of the wall-normal location of matching with the wall model, $y = y_{wm}$, as sketched in Figure 11. For instance, large values of y_{wm} located high in the log layer, far above the temperature peak (see Table 1), would most likely imply that the resolved field (with exception of the post-shock vibrational-relaxation layer, which is mostly inviscid) would consist of nonchemically reacting air in thermodynamic equilibrium, thereby rendering negligible chemical rates and energy exchanges. The endeavor of SGS modeling

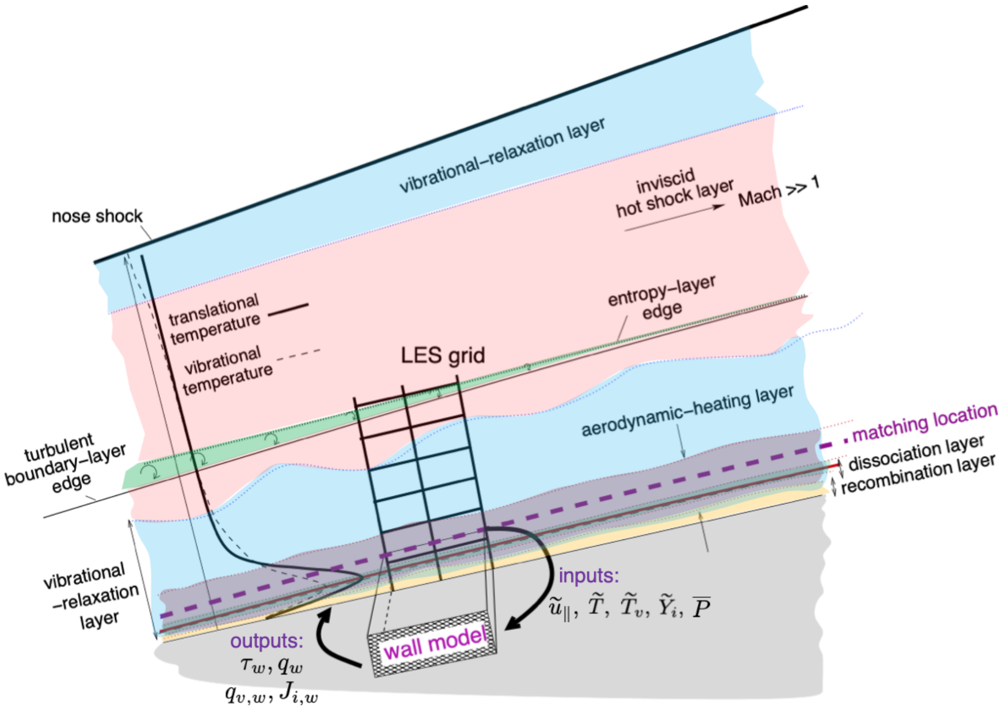
nose shock
vibrational–relaxation layer
inviscid hot shock layer
Mach >> 1
translational temperature
vibrational temperature
entropy–layer edge
LES grid
turbulent boundary–layer edge
aerodynamic–heating layer
matching location
dissociation layer
recombination layer
vibrational –relaxation layer
inputs:
$\widetilde{u}_{\parallel}$, $\widetilde{T}$, $\widetilde{T}_v$, $\widetilde{Y}_i$, $\overline{P}$
wall model
outputs:
τ_w, q_w
$q_{v,w}$, $J_{i,w}$

FIGURE 11. Schematics of a wall model for hypersonic turbulent flows at suborbital enthalpies.

for these source terms would, however, become unavoidably more important in the wall-modeled layer, where most of the interactions between turbulence and thermochemical effects occur.

A.3. *The wall model*

Equations (A 1)-(A 5) are subject to boundary conditions in the free stream $y \to \infty$ and on the wall $y = 0$. In wall-modeled LES, the boundary conditions on the wall for the resolved LES field consist of the wall values of the shear stress τ_w, species diffusion fluxes $J_{i,w}$, heat flux q_w, and vibrational heat flux $q_{v,w}$, whose expressions are given by

$$\tau_w = \widetilde{\mu}_w \left(\frac{\partial \widetilde{u}}{\partial y}\right)_w, \quad J_{i,w} = -\overline{\rho}_w \widetilde{Y}_{i,w} \widetilde{V}_{y,i,w}, \quad q_{v,w} = -\widetilde{\lambda}_{v,w} \left(\frac{\partial \widetilde{T}_v}{\partial y}\right)_w,$$

$$q_w = -\widetilde{\lambda}_w \left(\frac{\partial \widetilde{T}}{\partial y}\right)_w + \sum_{i=1}^{N_s} \overline{\rho}_w \widetilde{h}_{i,w} \widetilde{V}_{y,i,w} \widetilde{Y}_{i,w}. \tag{A 10}$$

The left-hand side of these expressions are obtained by integrating a set of wall-model equations within a modeled layer $0 \leq y \leq y_{wm}$. In writing these additional equations, a customary simplification near the wall is to neglect the mean convection of momentum and scalars, and the mean pressure gradients. Upon performing these simplifications and using the closure models in Eq. (A 8), the system of ordinary-differential equations

$$\frac{d}{dy}\left[(\mu+\mu_{t,w})\frac{du_{\|}}{dy}\right]=0, \tag{A 11}$$

$$\frac{d}{dy}\left(-\rho Y_i V_{y,i}+\frac{\mu_{t,wm}}{Sc_{t,i,wm}}\frac{dY_i}{dy}\right)+\dot{w}_i=0, \quad i=1,2\ldots N_s, \tag{A 12}$$

$$\frac{d}{dy}\left(\lambda_v\frac{dT_v}{dy}+\frac{\mu_{t,wm}}{Pr_{t,v,wm}}\frac{de_v}{dy}\right)+\dot{Q}_{v-t}=0, \tag{A 13}$$

$$\frac{d}{dy}\left[(\mu+\mu_t)u_{\|}\frac{du_{\|}}{dy}+\lambda\frac{dT}{dy}+\frac{\mu_{t,w}}{Pr_{t,wm}}\frac{dh}{dy}-\sum_{i=1}^{N_s}\rho h_i Y_i V_{y,i}\right]=0, \tag{A 14}$$

is obtained, which represents the wall-model conservation equations of momentum, species, vibrational internal energy, and static enthalpy. The density, temperature, and mass fractions are related by the equation of state (A 6), where the pressure is set to be uniform across the wall-modeled layer and equal to $\overline{P}$ at the matching location. The symbol $u_{||}$ is the total wall-parallel velocity in the wall-modeled layer, including both the streamwise and spanwise components.

The overline symbols, indicating filtering operators, have been removed in writing Eqs. (A 11)-(A 14) for consistency with early work and for distinguishing the variables in the wall-modeled layer from those in the LES conservation equations (A 1)-(A 5) for the resolved field. However, it should be emphasized that the variables in the wall-modeled layer represent both spatially and temporally averaged quantities: (a) spatially averaged over the spanwise and streamwise length of the LES grid cells close to the wall; and (b) temporally averaged over time scales comparable to the eddy turnover time y_{wm}/u_τ based on the matching location. As a result, it is important to notice that the chemical production rate $\dot{w}_i$ and the rate of energy exchange $\dot{Q}_{v-t}$ in the wall-model equations (A 12) and (A 13) are spatiotemporal averages of strongly non-linear functions of temperature, composition, and pressure. Consequently, their closure is not straightforward, as discussed above in Sections 3.4 and A.2.

In Eqs. (A 11)-(A 14), $\mu_{t,wm}$ is a wall-model eddy viscosity that could be specified according to the mixing-length model $\mu_{t,wm}=\kappa\rho y D(\tau_w/\rho)^{1/2}$ as usually done for low-speed flows, where $\kappa=0.42$ is the Kármán constant and $D=[1-\exp(-y^\star/A^+)]^2$ is a damping function, with $A^+=17$. Similarly, fixed values could be used for the wall-model eddy Prandtl and Schmidt numbers, for instance, $Pr_{t,wm}=Pr_{t,v,wm}=Sc_{t,i,wm}=0.9$, or spatial profiles obtained a-prori from DNS could be used instead (Di Renzo & Urzay 2021). However, the accuracy of these hypotheses has never been tested in hypersonic turbulent flows at high enthalpies.

The wall-model equations (A 11) and (A 14) are subject to

$$u_{||}=0, \quad T=T_v=T_w, \quad \text{and} \quad V_{y,i}=k_{i,w} \tag{A 15}$$

on the wall at $y=0$, where T_w is the wall temperature, and $k_{i,w}$ is the catalytic velocity, with $k_{i,w}=0$ representing a noncatalytic wall (Park 1990). The corresponding boundary conditions at the matching location $y=y_{wm}$ are

$$u_{||}=\widetilde{u}_{||}, \quad T=\widetilde{T}, \quad T=\widetilde{T}_v, \quad \text{and} \quad Y_i=\widetilde{Y}_i, \tag{A 16}$$

with $P=\overline{P}$, as mentioned above. In these expressions $\widetilde{u}_{||}$, $\widetilde{T}$, $\widetilde{T}_v$, $\widetilde{Y}_i$, and $\overline{P}$ are the resolved values of the wall-parallel velocity, translational temperature, vibrational temperature, species mass fractions, and pressure obtained from integrating Eqs. (A 1)-(A 5).

The wall model presented above can be simplified for a calorically perfect gas by neglecting Eqs. (A 12)-(A 13) along with the last term in Eq. (A 14), while using $h = c_pT = \gamma R_gT/(\gamma - 1)$ in Eq. (A 14), with γ being the adibatic coefficient. These simplifications lead to the standard wall model used in early work on compressible turbulent wall-bounded flows (Larsson *et al.* 2016), including shock-induced turbulence in low-enthalpy hypersonic boundary layers (Yang *et al.* 2018; Fu *et al.* 2021).

REFERENCES

Chen, S. Y. & Boyd, I. D. 2020 Boundary-layer thermochemical analysis during passive and active oxidation of silicon carbide. *J. Thermophys. Heat Trans.* **34**, 504–514.

Colonna, G., Bonelli, F. & Pascazio, G. 2013 Impact of fundamental molecular kinetics on macroscopic properties of high-enthalpy flows: The case of hypersonic atmospheric entry. *Phys. Rev. Fluids* **4**, 033404.

Chaudhry, R. S., Boyd, I. D., Torres, E., Schwartzentruber, T. E. & Candler, G. V. 2020 Implementation of a chemical kinetics model for hypersonic flows in air for high-performance CFD. *AIAA Paper* 2020-2191.

Di Renzo, M., Fu, L. & Urzay, J. 2020 HTR solver: An open-source exascale-oriented task-based multi-GPU high-order code for hypersonic aerothermodynamics. *Comput. Phys. Comm.* **255**, 107262.

Di Renzo, M. & Urzay, J. 2021 Direct numerical simulation of a hypersonic transitional boundary layer at suborbital enthalpies. *J. Fluid Mech.* (To Appear).

Duan, L. & Martin, M. P. 2011*a* Direct numerical simulation of hypersonic turbulent boundary layers. Part 4. Effect of high enthalpy. *J. Fluid Mech.* **684**, 25–59.

Duan, L. & Martin, M. P. 2011*b* Assessment of turbulence-chemistry interaction in hypersonic turbulent boundary layers. *AIAA J.* **49**, 172–184.

Finch, P. M., Girard, J., Strand, C., Yu, W., Austin, J., Hornung, H., Hanson, R. K. 2021 Measurements of time-resolved air freestream nitric oxide rotational, vibrational temperature and concentration in the T5 reflected shock tunnel. *AIAA Paper* 020-3714.

Fu, L., Karp, M., Bose, S., Moin, P. & Urzay, J. 2021 Shock-induced heating and transition to turbulence in a hypersonic boundary layer. *J. Fluid Mech.* **909**, A8.

Franko, K. J. & Lele, S. K. 2013 Breakdown mechanisms and heat transfer overshoot in hypersonic zero pressure gradient boundary layers. *J. Fluid Mech.* **730**, 491–532.

Goodrich, W., Derry, S. & Bertin, J. 1983 Shuttle Orbiter boundary-layer transition-A comparison of flight and wind tunnel data. *AIAA Paper* 83-0485.

Hader, C. & Fasel, H. F. 2019 Direct numerical simulations of hypersonic boundary-layer transition for a flared cone: fundamental breakdown. *J. Fluid Mech.* **869**, 341–384.

Happenheimer, T. A. 2007 Facing the heat barrier: A history of hypersonics. NASA SP-2007-4232.

Hank, J. M., Murphy, J. S. & Mutzman, R. C. 2008 The X-51A scramjet engine flight demonstration program. *AIAA Paper* 2008-2540.

Hillje, E. R. 2019 Entry aerodynamics at lunar return conditions obtained from the flight of Apollo 4 (AS-501). NASA TN-D-5399.

Jackson, K. R., Gruber, M. R. & Buccellato, S. 2015 Mach 6-8+ hydrocarbon-fueled scramjet flight experiment: The HIFiRE Flight 2 project. *J. Propul. Power* **31**, 36–53.

Johnson, H. B. & Candler G. V. 2005 Hypersonic boundary layer stability analysis using PSE-Chem. *AIAA Paper* 2005-5023.

Landau, L. V. & Teller, E. 1936 Zur theorie der schalldispersion. *Phys. Z. Sowjetunion* **10**, 34-43.

Larsson, J., Kawai, S., Bodart, J., Bermejo-Moreno, I. 2016 Large eddy simulation with modeled wall-stress: recent progress and future directions. *Mech. Eng. Rev.* **3**, 15-00418.

Marshall, L. Corpening, G. & Sherrill R. 2005 A chief engineer's view of the NASA X-43A scramjet flight test. *AIAA Paper* 2005-3332.

Marxen, O., Iaccarino, G. & Magin, T. E. 2014 Direct numerical simulations of hypersonic boundary-layer transition for a flared cone: fundamental breakdown. *J. Fluid Mech.* **755**, 35–49.

McBride, B. J., Zehe, M. J. & Gordon, S. 2002 NASA Glenn coefficients for calculating thermodynamic properties of individual species. NASA TP-2002-211556.

Moin, P., Squires, K., Cabot, W. & Lee, S. 1991 A dynamic subgrid-scale model for compressible turbulence and scalar transport. *Phys. Fluids* **3**, 2746–2757.

Mortensen, C. & Zhong, X. 2016 Real-gas and surface-ablation effects on hypersonic boundary-layer instability over a blunt cone. *AIAA J.* **56**, 4297–4311.

Park, C. 1989 A review of reaction rates in high temperature air. *AIAA Paper* 89-1740.

Park, C. 1990 *Nonequilibrium Hypersonic Aerothermodynamics.* John Wiley & Sons.

Peters, N. 2000. *Turbulent Combustion.* Cambridge University Press.

Pierce, C.D. & Moin, P. 2004. Progress-variable approach for large-eddy simulation of non-premixed turbulent combustion. *J. Fluid Mech.* **504**, 73-97.

Sayler, K. M. 2020 Hypersonic weapons: Background and issues for Congress. U. S. Congressional Research Service Report #R45811.

Singh N. & Schwartzentruber T. 2017 Nonequilibrium internal energy distributions during dissociation. *Proc. Natl. Acad. Sci. USA* **115**, 47-52.

Streicher, J. W., Krish, A., Hanson, R. K., Hanquist, K. M., Chaudhry, R. S. & Boyd, I. D. 2020 Shock-tube measurements of coupled vibration-dissociation time-histories and rate parameters in oxygen and argon mixtures from 5000 K to 10000 K. *Phys. Fluids* **32**, 076103.

Thome, J., Knutson, A. & Candler, G. V. 2019 Boundary layer instabilities on BoLT subscale geometry. *AIAA Paper* 2019-0092.

Urzay, J. 2018 Supersonic combustion in airbreathing propulsion systems for hypersonic flight. *Annu. Rev. Fluid Mech.* **50**, 593–627.

Urzay, J. 2020 *The Physical Characteristics of Hypersonic Flows.* ME356 Hypersonic Aerothermodynamics class notes. Center for Turbulence Research, Stanford University.

von Kármán, T. 1956 Aerodynamic heating. In Proc. Symp. *"High Temperature – a Tool for the Future."* Berkeley, California.

Watts, J. D. 1968 Flight experience with shock impingement and interference heating on the X-15A2 research airplane. NASA TM-X-1669.

Yang, X.I.A., Urzay, J., Bose, S. T. & Moin, P. 2018 Aerodynamic heating in wall-modeled large-eddy simulation of high-speed flows. *AIAA J.* **56**, 731–742.

Zhang, C., Duan, L. & Choudhari, M. M. 2018 Direct numerical simulation database for supersonic and hypersonic turbulent boundary layers. *AIAA J.* **56**, 4297–4311.